Giant ankyrin-G: A critical innovation in vertebrate evolution of fast and integrated neuronal signaling

Paul M. Jenkins[a,b], Namsoo Kim[c], Steven L. Jones[d], Wei Chou Tseng[e], Tatyana M. Svitkina[d], Henry H. Yin[c], and Vann Bennett[a,b,f,1]

[a]Howard Hughes Medical Institute and [b]Department of Biochemistry, [c]Department of Psychology and Neuroscience, [e]Department of Pharmacology and Cancer Biology, [f]Departments of Cell Biology and Neurobiology, Duke University Medical Center, Durham, NC 27710; and [d]Department of Biology, University of Pennsylvania, Philadelphia, PA 19104

This article is part of the special series of Inaugural Articles by members of the National Academy of Sciences elected in 2010.

Edited by William A. Catterall, University of Washington School of Medicine, Seattle, WA, and approved December 5, 2014 (received for review August 27, 2014)

Axon initial segments (AISs) and nodes of Ranvier are sites of clustering of voltage-gated sodium channels (VGSCs) in nervous systems of jawed vertebrates that facilitate fast long-distance electrical signaling. We demonstrate that proximal axonal polarity as well as assembly of the AIS and normal morphogenesis of nodes of Ranvier all require a heretofore uncharacterized alternatively spliced giant exon of ankyrin-G (AnkG). This exon has sequence similarity to I-connectin/Titin and was acquired after the first round of whole-genome duplication by the ancestral *ANK2/ANK3* gene in early vertebrates before development of myelin. The giant exon resulted in a new nervous system-specific 480-kDa polypeptide combining previously known features of ANK repeats and β-spectrin–binding activity with a fibrous domain nearly 150 nm in length. We elucidate previously undescribed functions for giant AnkG, including recruitment of β4 spectrin to the AIS that likely is regulated by phosphorylation, and demonstrate that 480-kDa AnkG is a major component of the AIS membrane "undercoat" imaged by platinum replica electron microscopy. Surprisingly, giant AnkG-knockout neurons completely lacking known AIS components still retain distal axonal polarity and generate action potentials (APs), although with abnormal frequency. Giant AnkG-deficient mice live to weaning and provide a rationale for survival of humans with severe cognitive dysfunction bearing a truncating mutation in the giant exon. The giant exon of AnkG is required for assembly of the AIS and nodes of Ranvier and was a transformative innovation in evolution of the vertebrate nervous system that now is a potential target in neurodevelopmental disorders.

neuropsychiatric disease | cognitive impairment disorder | axon initial segment | ankyrin-G | axonal polarity

By the beginning of the Devonian period, 420 million years ago, jawed fish had evolved excitable axonal membrane microdomains, termed axon initial segments (AISs) and nodes of Ranvier, which allowed small caliber axons to generate and rapidly conduct action potentials (APs) over long distances (1). This pivotal innovation was a major factor in the extraordinary success of vertebrates by enabling our ancestors to develop miniaturized but highly integrated central nervous systems while achieving unprecedented body sizes. AISs, in addition to generating APs, also are innervated by GABAergic axo-axonic interneurons, which are key elements in neural circuits (2). AISs are capable of plasticity in response to neural activity and may have a role in adaptive responses of the nervous system, including some forms of learning and memory (3, 4). AISs also are involved in epilepsy as well as major psychiatric diseases (5).

Axonal excitable membrane domains attracted the interest of pioneering electrophysiologists and electron microscopists as sites associated with sodium-based APs that were coated with distinctive submembranous fibrillar material (6, 7). Resolution of the protein composition of these domains began with the discovery that both AIS and nodes of Ranvier are endowed with high local concentrations of voltage-gated sodium channels (VGSCs) (8). VGSCs copurified with membrane skeletal proteins, leading to the discovery that these channels associated directly and colocalized with the ankyrin family of membrane adaptors (9–11). The prototype ankyrin in erythrocytes couples the anion exchanger to a membrane-associated spectrin-actin network, suggesting the possibility of a similar function in stabilizing VGSC assemblies in the axon (12–15).

Ankyrin-G (AnkG) (product of the *ANK3* gene) was identified as the VGSC-associated ankyrin (16) and was demonstrated, based on targeted cerebellar knockout in mice, to be essential for VGSC clustering at the AIS and for normal AP firing in vivo (17, 18). In a departure from the simple erythrocyte membrane, AnkG also directly interacts with and coordinates other components of the AIS, including a 186-kDa alternatively spliced variant of neurofascin, an L1 family cell adhesion molecule that directs GABAergic synapses to the AIS (17–22), β4 spectrin, a member of the β-spectrin family that stabilizes the AIS and nodes of Ranvier (23, 24), and KCNQ2/3 voltage-gated potassium channels that modulate sodium channel excitability (25). Moreover, AnkG promotes microtubule bundles and the submembrane material noted at the AIS by transmission electron microscopy (26). Consistent with these findings that multiple AIS proteins depend on AnkG, AnkG-null axons acquire dendritic properties in their proximal segments, both in cultured neurons as well as in mice (26, 27). AnkG thus is a master organizer of the

Significance

Excitable axonal membrane microdomains are unique features of vertebrate nervous systems that are required for normal neuronal signaling and are involved in human neurological disorders. Ankyrin-G is a critical adaptor protein that acquired a giant exon early in vertebrate evolution, resulting in a new nervous system-specific polypeptide that is a master organizer of axonal excitable membranes. Giant ankyrin-G–deficient mice live to weaning and provide a rationale for survival of humans with severe cognitive dysfunction bearing a truncating mutation in the giant exon. The giant exon of ankyrin-G thus was a transformative innovation in evolution of the vertebrate nervous system that now is a potential target in neurodevelopmental disorders.

Author contributions: P.M.J., T.M.S., H.H.Y., and V.B. designed research; P.M.J., N.K., S.L.J., and W.C.T. performed research; P.M.J., N.K., S.L.J., T.M.S., H.H.Y., and V.B. analyzed data; and P.M.J. and V.B. wrote the paper.

The authors declare no conflict of interest.

This article is a PNAS Direct Submission.

[1]To whom correspondence should be addressed. Email: vann.bennett@duke.edu.

This article contains supporting information online at www.pnas.org/lookup/suppl/doi:10.1073/pnas.1416544112/-/DCSupplemental.

www.pnas.org/cgi/doi/10.1073/pnas.1416544112

AIS (5, 28). Nodes of Ranvier, which evolved later than the AIS (29), share a similar AnkG-based interactome but require axonal–glial interactions as well as extracellular matrix for their formation (reviewed in ref. 30).

A 480-kDa isoform of AnkG contains residues encoded by a vertebrate-specific giant 7.8-kb exon that is expressed in the nervous system (16, 31). This vertebrate exon is at a different site and distinct from the inserted sequence found in Drosophila giant ankyrin (32). The giant exon was acquired after the first round of whole-genome duplication by the ancestral *ANK2*/*ANK3* gene in early jawless vertebrates before development of myelin (31). In addition, the exon also encodes a 40-kDa serine- and threonine-rich subdomain that is modified by O-linked *N*-acetylglucosamine (33) and has minimal sequence similarity to other proteins. The AnkG giant exon is conserved between humans and zebrafish, indicating strong evolutionary pressure to maintain sequence and preserve an uninterrupted exon.

Although giant exons of ankyrin-B and AnkG were discovered over 20 y ago (16, 34, 35), relatively little is known about their function. The 270-kDa AnkG, resulting from an in-frame splicing event that eliminates 1,900 amino acids from the giant exon, retains the ability to target to the AIS of WT neurons (36–39) as well as AnkG-deficient neurons (40). However, potential functions of the remaining 1,900 amino acids have not been examined. Interestingly, a frame-shift mutation in this region predicted to disrupt 480-kDa AnkG associates with severe cognitive disability in humans (41). mRNA levels of the 480-kDa AnkG isoform are dramatically reduced in lymphoblastoid cells, indicating that individuals homozygous for the mutation likely completely lack 480-kDa AnkG (41). Although these patients exhibit major intellectual disability (IQ < 50), hypotonia, spasticity, and severe behavioral problems, 480-kDa AnkG is not essential for viability.

Here, we report functional characterization of 480-kDa AnkG and present evidence from cultured neurons and mutant mice for a critical role of its giant exon-encoded sequence in formation of the AIS as well as central nervous system (CNS) nodes of Ranvier. We further demonstrate that the giant exon is required for assembly of β4 spectrin at the AIS and that this recruitment is potentially regulated by phosphorylation. We also critically evaluate a proposed role of the AIS as a selective filter separating axonal and dendritic compartments (28). Remarkably, we find that, similar to humans with a truncating mutation, mice lacking the giant exon survive to weaning and can generate evoked APs, although with reduced frequency and abnormal alpha and gamma oscillations.

Results

The AIS of Cultured Neurons Requires 480-kDa AnkG. We initially explored the role of 480-kDa AnkG at the AIS of cultured hippocampal neurons by expression of shRNA specific for this 480-kDa isoform that spares the shorter 270- and 190-kDa AnkG polypeptides (Fig. S1). Strikingly, specific knockdown of 480-kDa AnkG completely abolished AnkG staining at the AIS as well as clustering of its associated binding partners, β4 spectrin, VGSC, and NF186 (Fig. S1). To address the role of the giant exon (exon 37) in more detail, we generated a full-length cDNA encoding the 480-kDa AnkG isoform tagged with GFP, developed antibodies specific to the 480-kDa isoform, and established methods to perform structure–function studies of AnkG isoforms in AnkG-null hippocampal neurons. A 480-kDa AnkG-GFP cDNA was generated using a chemically synthesized sequence encoding the giant exon of rat AnkG identified in the rat genome based on exon 37 of the human giant ANK3 transcript, and subcloned into the 190-kDa rat AnkG-GFP plasmid, described previously (42).

Previous studies of the function of AnkG at the AIS have used WT neurons (36–39, 43), which have a full complement of AnkG-dependent binding partners. To address the structural requirements of AnkG in recruiting these proteins in an AnkG-null background, we used cultured hippocampal neurons from mice containing loxP sites flanking exons 22 and 23 that lose all known AnkG isoforms after expression of Cre recombinase (44) (Fig. 1*A*). Importantly, Cre recombinase expression in neurons at 3 days in vitro completely abolishes AIS clustering of AnkG as well as β4 spectrin, VGSC, and NF186, (Fig. 1*B* and Fig. S2).

Rescue of AnkG-null neurons with 480-kDa AnkG cDNA completely restored clustering of AnkG at the AIS, both in

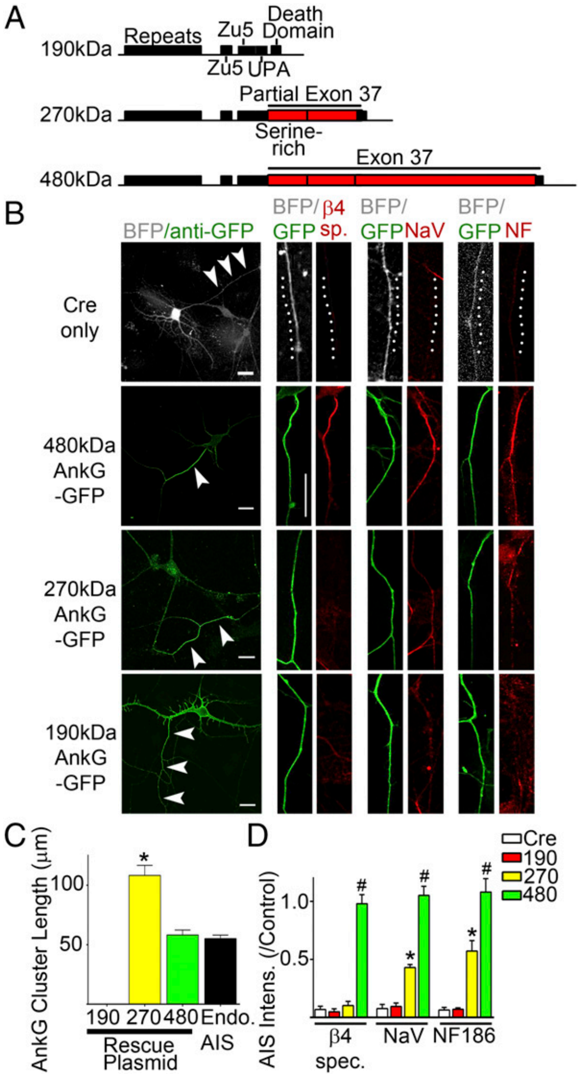

Fig. 1. The entire giant ankyrin-G insert is necessary for clustering of AISs. (*A*) Representation of the AnkG transcripts with giant inserted exon 37 marked in red. (*B*) Representative images of cultured total AnkG-null hippocampal neurons (*Top*) or those rescued with indicated GFP constructs. Arrowheads denote axon. Blue fluorescent protein (BFP) signal for Cre only neurons shown in white and anti-GFP shown in green. Clustering of AIS components β4 spectrin, VGSC (NaV), and NF186 (NF) shown on right in red. (Scale bars: 20 μm.) (*C*) Quantification of length of AnkG-GFP clustering from *B* compared with endogenous AIS (Endo. AIS). $^{*}P < 0.05$ compared with 480-kDa AnkG rescue and endogenous axon initial segments (one-way ANOVA, $P < 0.0001$, Tukey post hoc test, $n = 18–23$ per group). (*D*) Quantification of mean fluorescence intensity of AIS of total AnkG-null hippocampal neurons rescued with indicated constructs relative to untransfected controls. $^{*}P < 0.05$ relative to Cre alone and 190-kDa AnkG-GFP; $^{\#}P < 0.05$ relative to Cre alone, 190-kDa, and 270-kDa AnkG-GFP (one-way ANOVA, $P < 0.0001$, Tukey post hoc test, $n = 5–7$ for each group).

length (Fig. 1 *B* and *C*) and in position relative to the soma (Fig. 1*B* and Fig. S2), rendering AnkG staining indistinguishable from that of untransfected control cells (Fig. 1 *B* and *C* and Fig. S3). In addition, rescue with 480-kDa AnkG completely restored localization of known AIS binding partners, β4 spectrin, VGSC, and NF186 (Fig. 1 *B* and *D*). In contrast, 190-kDa AnkG did not cluster within the proximal axon or restore localization of AnkG binding partners (Fig. 1 *B–D*). As shown previously, 270-kDa AnkG does cluster in the axon (40). However, 270-kDa AnkG clusters were longer than the endogenous AIS and located more distally (Fig. 1 *B* and *C* and Fig. S3). In addition, 270-kDa AnkG restored VGSC and NF186 localization in an AnkG-null background, but with reduced intensity relative to endogenous levels (Fig. 1 *B* and *D*).

Surprisingly, 270-kDa AnkG completely failed to restore β4 spectrin localization to the AIS even though 480-kDa AnkG was fully active (Fig. 1 *B* and *D*). This lack of β4 spectrin recruitment was unexpected because 270-kDa AnkG is capable of interacting with β4 spectrin in immunoprecipitation experiments (24, 37) and because the canonical spectrin-binding site located in the first ZU5 domain is shared by all AnkG isoforms (45, 46). We therefore examined whether 480-kDa AnkG requires its ZU5 domain spectrin-binding site by evaluating activity of the DAR999AAA mutation, which abolishes known ankyrin–spectrin interactions (47). Interestingly, DAR999AAA mutation 480-kDa AnkG had no effect on its ability to cluster in the proximal axon (Fig. S3) or to recruit binding partners, including β4 spectrin, to the AIS (Fig. 2 *B* and *C*). These results demonstrate that recruitment of β4 spectrin to the AIS occurs independently of the canonical spectrin–ankyrin interaction site located in the first ZU5 domain.

Using alanine-scanning mutagenesis of the giant exon of AnkG, we discovered that a S2417A mutation (corresponding to position 2417 in human AnkG) dramatically reduced its ability to recruit β4 spectrin to the AIS (Fig. 2). Interestingly, this S2417A mutation had no effect on clustering of the AnkG protein itself (Fig. S3) or recruitment of NF186 or the VGSC (Fig. 2 *B* and *C*). S2417 is a predicted casein kinase 2 (CK2) phosphorylation site, and CK2 has been demonstrated to increase VGSC binding to AnkG (48). The phosphomimetic S2417D mutation fully restores 480-kDa AnkG's ability to recruit β4 spectrin to the AIS (Fig. 2 *B* and *C*), which is consistent with a role for phosphorylation of S2417 in activating β4 spectrin recruitment.

Overall, these results demonstrate that 480-kDa AnkG is required for full reconstitution of the AIS whereas 270-kDa AnkG has only partial activity, and 190-kDa ANK-G is completely inactive. Moreover, 480-kDa AnkG recruits β4 spectrin through an interaction likely regulated by phosphorylation at S2417, which is located in the 1,900 amino acid region that is missing from 270-kDa AnkG.

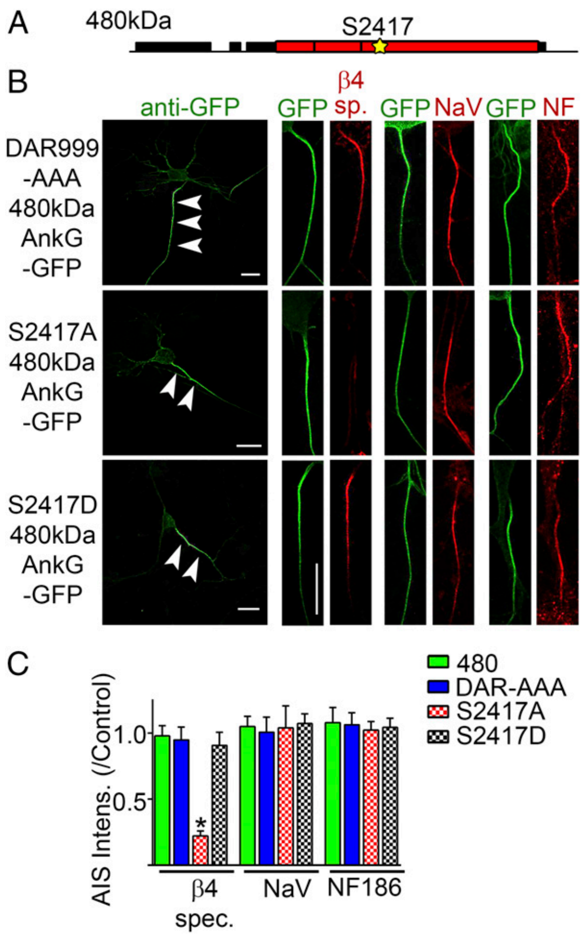

Fig. 2. β4 spectrin is recruited to the AIS through a noncanonical interaction with ankyrin-G that is likely regulated by phosphorylation. (*A*) Representation of the 480-kDa AnkG transcript with the location of S2417 marked by a yellow star. (*B*) Representative images of cultured exon 22/23-null hippocampal neurons rescued with indicated constructs. Arrowheads denote axon. Anti-GFP shown in green. AIS partners shown on right in red. (Scale bars: 20 μm.) (*C*) Quantification of mean fluorescence intensity of AIS partners. $^*P < 0.05$ relative to 480-kDa AnkG-GFP (one-way ANOVA, $P < 0.0001$ followed by Tukey post hoc test, $n = 5–7$ for each group). Note: Data from 480-kDa AnkG-GFP rescue from Fig. 1*D*.

Genetic Deletion of the Giant Exon Eliminates the AIS in Vivo. Previous studies of neuronal roles of AnkG in vivo have deleted all AnkG polypeptides in the postnatal cerebellum (17, 18, 26). To specifically examine the role of 480-kDa AnkG, we generated mice, with loxP sites flanking the giant exon, that were crossed with mice expressing Cre under control of the Nestin promoter in neuronal and glial precursors (Fig. 3*B*). Importantly, genetic deletion of the giant exon would be expected to spare function of the 190-kDa isoform of AnkG in regulating the size of dendritic spines and AMPA receptor plasticity (49). These mice exhibited loss of the giant exon-encoded sequence from the majority of brain areas examined, while sparing expression in the dentate gyrus, optic nerve, sciatic nerve, and the majority of the spinal cord (Figs. 3 and 4 and Fig. S4).

Surprisingly, giant exon-null mice survived through weaning, living up to 20 d, whereas total AnkG-null mice crossed with the same nestin-Cre line died immediately after birth (Fig. 3*C*). Western blots from whole-brain lysates confirmed a >90% loss of 480- and 270-kDa giant AnkG isoforms (Fig. 3*D*). However, giant exon-null mice had a four- to fivefold increase in expression of 190-kDa AnkG as well as a 210-kDa splice variant containing an additional 195 amino acids (50). We did not detect any changes in levels of ankyrin-B or -R isoforms or known AnkG binding partners, including VGSC, β4 spectrin, or NF186 (Fig. S5).

Immunolabeling of p20 brain sections with either antibodies specific to the 480-kDa isoform of AnkG or reacting with all AnkG polypeptides revealed a complete loss of AnkG immunoreactivity at the AIS in nearly all areas of giant exon-null brains, including the cortex (Fig. 3*E*, *Top*), cerebellum (Fig. 3*F*), CA1-3 of the hippocampus, and the striatum, consistent with the >90% loss of protein seen by Western blot (Fig. 3*D*). Thus, giant exon-null animals completely lack recruitment of AnkG to the AIS even though smaller isoforms were increased (Fig. 3*D*).

In addition to missing AnkG labeling at the AIS, giant exon-null mice lost known AIS proteins, including β4 spectrin, NF186, VGSC, and KCNQ2 (Fig. 3*E*). Moreover, consistent with results from the total AnkG-null cerebellum (19), Pinceau GABAergic synapses on the AIS of Purkinje neurons were almost completely absent (Fig. 3*F*). Interestingly, the proximal axon increased in diameter (Fig. 3*F*), and the dendritic marker MAP2 invaded the

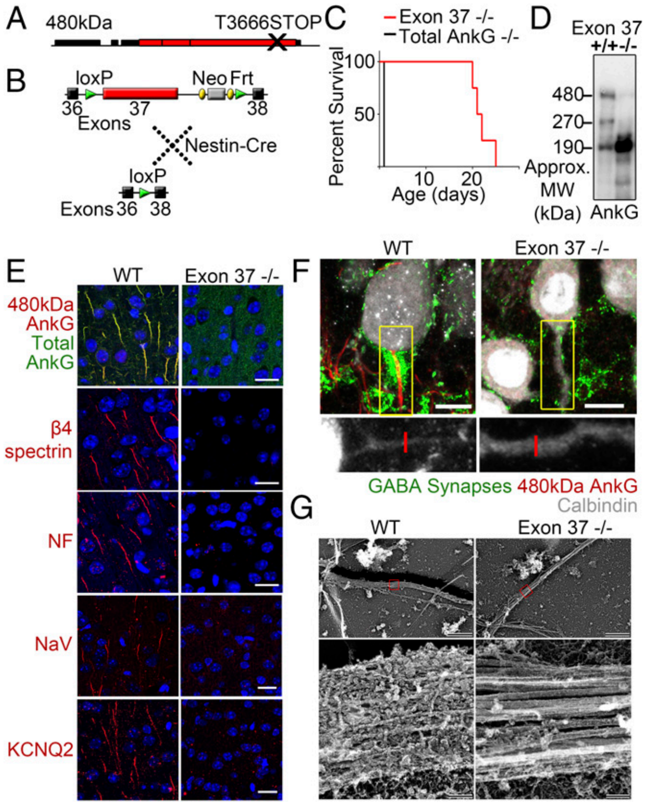

Fig. 3. Deletion of the giant insert of ankyrin-G causes a complete loss of known AIS components. (*A*) Representation of the 480-kDa AnkG transcript with location of the premature stop at T3666 (41) marked by black ×. (*B*) Strategy for genetic deletion of the giant AnkG exon. (*C*) Survival curve from giant AnkG-null (exon 37 –/–, red) or total AnkG-null (exon 22/23 –/–, black) mice. (*D*) Western blot of whole brain lysate from p20 WT (+/+) and exon 37-null (–/–) mice probed with total AnkG antibodies. (*E*) Representative images from coronal sections of p20 WT (*Left*) or exon 37–/– (*Right*) layer II/III cortex. AIS partners shown in red [480-kDa AnkG, NF186, NaV (VGSC), and KCNQ2]. (*Top*) Includes immunolabeling for total AnkG shown in green. Dapi shown in blue. (Scale bars: 20 μm.) (*F*) Representative images of cerebellar sections from WT (*Left*) or exon 37 –/– (*Right*) mice stained with antibodies to the GABAergic synapse marker VGAT (green), 480-kDa AnkG (red), and Purkinje cell marker calbindin (white). Higher magnification image of calbindin from region of interest shown *Below*. Red bar denotes width of exon 37 –/– proximal axon. (Scale bars: 10 μm.) (*G*) Platinum replica electron micrographs of the proximal axon of WT (*Left*) and exon 37-null (*Right*) cultured hippocampal neurons at 7 DIV showing complete loss of the fibrillogranular coat. Higher magnification images of red regions of interest shown on *Bottom*. (Scale bars: *Top*, 2 μm; *Bottom*, 100 nm.)

proximal axon, similar to disruption in proximal axo-dendritic polarity observed in total AnkG-null neurons (26, 27). Dendrite-like spines, previously noted in proximal axons of postnatal day 28 to 35 AnkG-null Purkinje neurons (26), were not evident in these postnatal day 16 to 20 mice. We therefore examined DIV21 hippocampal cultures from giant exon-null mice (Fig. S6). Strikingly, these cultures fully reproduce the dramatic loss of polarity of the proximal axon reported by Rasband and coworkers in total AnkG-null neurons, including MAP2 invasion and formation of dendritic spines (Fig. S6) (26, 27).

Platinum replica electron microscopy of dissociated hippocampal neurons from giant exon-null mice revealed complete loss of the submembranous fibrillogranular coat recently resolved by Svitkina and coworkers (51) (Fig. 3*G*). In addition, tight bundling of the microtubules was lost. These data demonstrate that the giant 480-kDa isoform of AnkG is essential for formation of the AIS in vivo as well as in cultured neurons.

Major CNS Node of Ranvier Malformation with Loss of Giant Exon. Although the AIS and nodes of Ranvier represent critical sites of clustering of VGSCs and share very similar protein composition, their mechanisms of assembly are different. The AIS forms autonomously and requires only neuronal AnkG for recruitment of all of the downstream binding partners (5). However, nodes of Ranvier require participation of glial cells and neurons where glial NF155 assembles the axoglial junction, and the neuronal NF186 isoform clusters AnkG at the node, followed by subsequent secondary recruitment of VGSCs (reviewed in ref. 30). In addition, other mechanisms participate in node assembly, including glial-derived extracellular matrix-mediated clustering of NF186, restriction of nodal protein mobility through a paranodal barrier, and stabilization of nodal proteins through interactions with the cytoskeleton (52, 53).

Analysis of the corpus callosum of giant exon-knockout mice revealed an 80% reduction in the number of nodes of Ranvier and a concomitant increase in isolated Caspr-positive axo-glial junctions (Fig. 4 *A* and *B*). These isolated paranodes were not found in obvious pairs along the same axonal tract and likely represent a state of stalled or delayed biogenesis. In addition, remaining nodes of Ranvier lacked 480-kDa AnkG (Fig. 4*A*, *Top*) and were markedly malformed, with greatly increased lengths, sometimes greater than 20 μm (Fig. 4*C*). Interestingly, 190-kDa AnkG still clustered at elongated nodes (Fig. 4*A*). Neurofascin, presumably NF155 (54), persisted in giant exon-knockout paranodes (Fig. 4*A*). In contrast, nodal neurofascin was completely lost from the remaining nodes of Ranvier (Fig. 4*A*). Despite the loss of nodal neurofascin, β4 spectrin and the VGSC were recruited to the remaining nodes (Fig. 4*A*). The nodal VGSC could be a result of persistent clustering of 190-kDa AnkG at the node, stabilization of the VGSC by the axoglial junctions through the remaining paranodal neurofascin (53), or

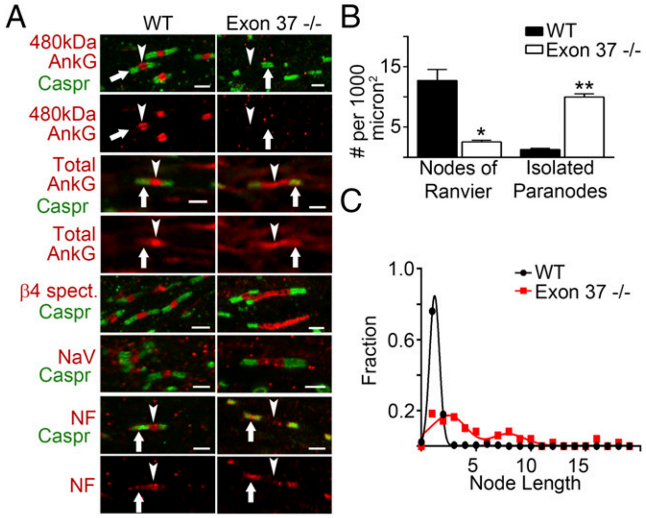

Fig. 4. Loss of giant ankyrin-G causes a dramatic reduction in the number of nodes of Ranvier and malformation of remaining nodes. (*A*) Representative images of nodes of Ranvier from the corpus callosum of p20 WT (*Left*) and exon 37-null (*Right*) brains. Caspr shown in green. Nodal proteins are shown in red. (Scale bars: 2 μm.) Arrowheads denote node of Ranvier. Arrows denote paranode. (*B*) Number of nodes of Ranvier (*Left*) or isolated paranodes (*Right*) per 1,000 μm^2 in corpus callosum from p20 WT (filled bars) or exon 37-null (open bars). *$P = 0.0053$ (WT, 12.7 ± 1.8, $n = 3$; exon 37-null, 2.5 ± 0.3, $n = 3$). **$P < 0.0001$ (WT, 1.3 ± 0.2, $n = 3$; exon 37-null, 10.0 ± 0.5, $n = 3$). Data shown are mean ± SEM. (*C*) Histogram node of Ranvier length from corpus callosum of p20 WT (black) and exon 37-null (red) brains (WT, $n = 167$, mean length 1.3 ± 0.1 μm; exon 37-null, $n = 49$, mean length 5.1± 0.6 μm).

through secretion of soluble factors from oligodendrocytes or astrocytes. Although a majority of axons in the spinal cord, the sciatic nerve, and optic nerve were not affected by Nestin-Cre, as indicated by the continued expression of giant AnkG, similar results were obtained from the subset of spinal axons lacking giant AnkG (Fig. S4).

Interestingly, 190-kDa AnkG present at remaining nodes is unable to cluster NF186 in the corpus callosum (Fig. 4, 25/25 nodes) or in the spinal cord (Fig. S4, 10/11 elongated nodes), despite the presence of the neurofascin-binding site in the membrane-binding domain (55). It is possible that NF186 is phosphorylated on its FIGQY motif, preventing the association with AnkG (56, 57). Because nestin-Cre removes the giant exon from both neuronal and glial precursors, giant ankyrin isoforms may function in myelinating glia as well as neurons (58). In addition, we cannot exclude the possibility of a dominant-negative effect of overexpression of 190-kDa AnkG.

The AIS Is Not Required for Maintenance of the Distal Axon. The AIS has been proposed to physically separate somatodendritic and axonal compartments through limiting diffusion both in the plane of the plasma membrane (59) and within the axoplasm (43) (reviewed in refs. 5 and 28). Indeed, deletion of AnkG polypeptides associated with loss of the AIS causes the proximal axon to exhibit dendritic properties including acquisition of dendritic spines and localization of marker proteins, such as MAP2 (26, 27) (Fig. S6). However, in both giant exon-null (Fig. 5*A*) and total AnkG-null (Fig. S3*B*) hippocampal cultures, axonal character resumes ∼50–100 μm from the soma. Even with extended culture of the exon 37-null neurons to 21 days in vitro, MAP2 still was excluded from the distal axon (Fig. 5*B* and Fig. S6). Interestingly, there was a trend in extension of MAP2 further down the axon between days 14 and 21, suggesting the possibility of a slow loss of axonal polarity with time in neurons lacking giant AnkG (Fig. 5*B*).

An important prediction from both the plasma membrane and axoplasmic filter models is that dendritic and axonal cargos would be randomized in the absence of the AIS. We therefore determined the behavior of the dendritic cargos transferrin receptor and TGN38 in AnkG-null neurons (Fig. 5 *C* and *D*). Both of these dendritic proteins maintain their polarized localization to dendrites and are excluded from the distal axon (Fig. 5 *C* and *D*) despite complete loss of all detectable AIS features (Fig. 3). Lysosomes are relatively large (50-500 nm) and are predicted to be affected by the diffusion limit of the proposed cytoplasmic "filter" (43). However, anterograde and retrograde transport rates of the lysosomal protein LAMP-1 were identical in the AIS (first 50 μm of the axon) compared with the distal axon (distal 100 μm) in dissociated hippocampal cultures (Fig. 5 *E* and *F*). In addition, complete loss of the AIS in total AnkG-null neurons also had no detectable effect on lysosomal transport (Fig. 5 *E* and *F*). These observations are consistent with the recent finding of unaltered rates of NgCAM transport between the AIS and distal axon (60). Together, these data demonstrate that distal axonal polarity is maintained despite the complete loss of the AIS. Neurons thus must possess AIS-independent mechanisms to establish and maintain distinct axonal and dendritic compartments.

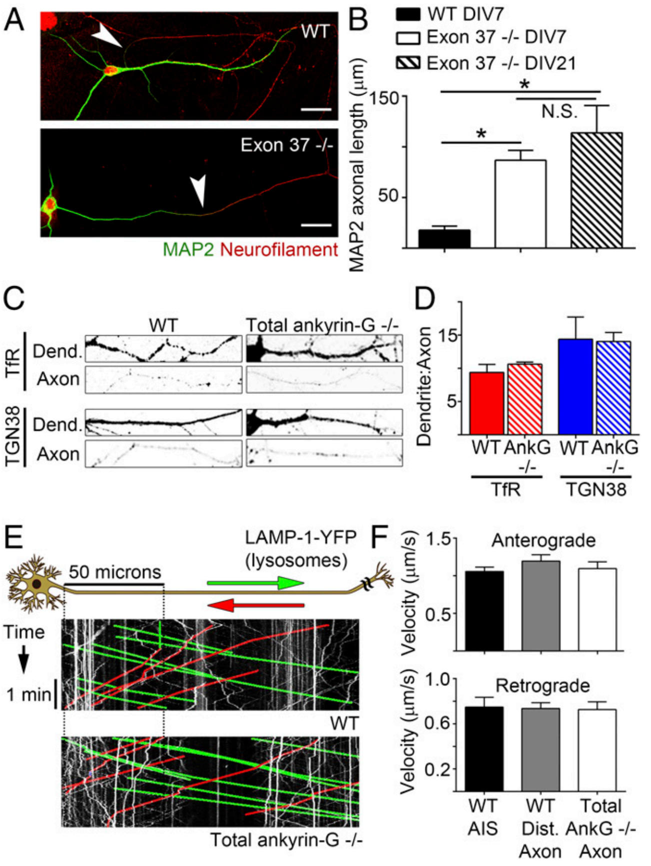

Fig. 5. Rate of axonal transport and steady-state localization of dendritic proteins is unaffected by loss of AIS. (*A*) Representative images of DIV8 cultured hippocampal neurons from WT (*Top*) or exon 37-null (*Bottom*) mice. The dendritic marker MAP2 is shown in green, and the axonal marker neurofilament is shown in red. Transition from dendritic character to axonal character marked by arrowhead. (Scale bars: 20 μm.) (*B*) Average distance of MAP2 invasion in DIV7 or DIV21 exon 37 –/– compared with control (one-way ANOVA, $P < 0.04$ followed by Tukey post hoc test, $n = 4$–13 for each group, *$P < 0.05$, N.S., not significant. (*C*) Representative images of steady-state localization of the dendritic cargos, transferrin receptor-YFP (TfR, *Top*) or TGN38-YFP (*Bottom*) to dendrites and distal axons from WT (*Left*) or total AnkG-null (*Right*) DIV7 hippocampal cultures. (*D*) Quantification of dendrite to axon fluorescence intensity ratio of TfR-YFP (red) or TGN38-YFP (blue) in WT (solid) or total AnkG-null (hatched) DIV7 hippocampal neurons (TfR, $P = 0.35$; WT, 9.4 ± 1.2, $n = 5$; total AnkG-null, 10.6 ± 0.33, $n = 5$; TGN38, $P = 0.9145$; WT, 14.4 ± 3.3, $n = 4$; total AnkG-null, 14.0 ± 1.4, $n = 6$). (*E*) Kymograph analysis of lysosomal (LAMP-1-YFP) movement through and past the AIS from WT (*Top*) or total AnkG-null (exon 22/23 –/–, *Bottom*) cultured hippocampal neurons. (Scale bars: 1 min for *y* axis and 50 μm for *x* axis.) Dotted lines represent length of average AIS (∼50 μm) on kymograph. (*F*) Quantification of velocity of LAMP1-YFP in the anterograde (*Top*) or retrograde (*Bottom*) direction for the WT AIS (black, first 50 μm), WT distal axon (gray, 50–150 μm), or total AnkG-null proximal axon (white, first 50 μm).

Elicited Action Potentials Persist with Complete Loss of the AIS. Multiple studies have concluded that AIS and/or the first node of Ranvier are required for AP generation (reviewed in ref. 61). However, knockout of all AnkG isoforms and subsequent loss of the AIS in the cerebellum impairs, but does not eliminate, AP production (18). Moreover, loss of 480-kDa AnkG in human patients is compatible with life (41) whereas giant exon-knockout mice with complete loss of known AIS features (Fig. 3) survive until postnatal day 20. To address the ability of neurons lacking an AIS to generate APs, we compared APs evoked through somatic current injection in acute slices of cortex (Fig. 6) or striatum (Fig. S7) from postnatal day 20 giant exon-null mice and WT littermates.

Surprisingly, current injection-induced APs persisted in the giant exon-null cortex (Fig. 6 *A*–*D*) and striatum (Fig. S7). Moreover, despite the complete loss of detectable clustering of VGSCs at the AIS (Fig. 3*E*), AP amplitudes were unchanged in cortex (*t* test, $P = 0.0813$, WT, 100.0 ± 1.9 mV, $n = 10$; exon 37-null, 106.5 ± 3.0 mV, $n = 10$) or striatum (*t* test, $P = 0.9587$, WT, 103.2 ± 4.1 mV, $n = 10$; exon 37-null, 103.5 ± 3.5 mV, $n = 10$).

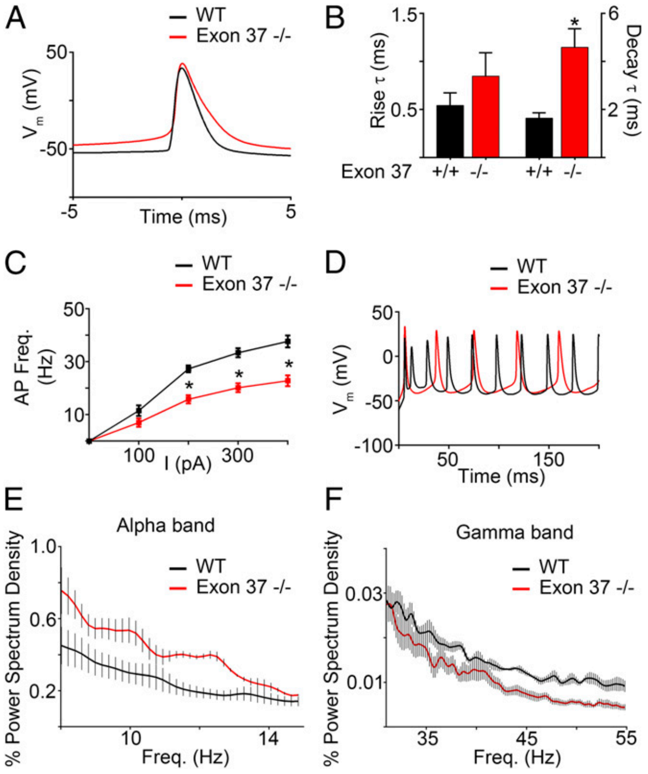

Fig. 6. APs persist in the exon 37-null mouse, although with altered dynamics and differences in integrated signaling. (*A*) Representative aligned single AP traces from WT (black) or exon 37-null (red) cortical neurons at +400 pA current injection. (*B*) Time constants (τ) for AP rise (*Left*) or decay (*Right*) from WT (black) or exon 37-null (red) at +400 pA current injection (rise τ, WT, 0.5 ± 0.1, $n = 10$; exon 37-null, 0.8 ± 0.2, $n = 10$; decay τ, $^*P < 0.05$, WT, 1.6 ± 0.2, $n = 10$; exon 37-null, 4.6 ± 0.8, $n = 10$). (*C*) Elicited AP frequency from cortical neurons from WT (black) or exon 37-null (red) acute brain slices. Data shown are mean ± SEM, $^*P < 0.05$ compared with WT. (*D*) Representative AP traces from cortical neurons from WT (black) or exon 37-null (red) at +400 pA current injection. (*E*) Relative alpha band (8–15 hz) local field potential power spectrum of awake p20 WT (black) or exon 37-null (red) mice plotted as a percentage of total EEG power spectrum. Data shown are mean ± SEM from three mice (five sessions total for each genotype). (*F*) Relative gamma band (32–55 hz) local field potential power spectrum of awake p20 WT (black) or exon 37-null (red) mice plotted as a percentage of EEG power spectrum. Data shown are mean ± SEM from three mice (five session total for each genotype).

Current input required to elicit an AP also was unchanged in cortex (*t* test, $P = 0.5560$, WT, 110 ± 10 pA, $n = 10$; exon 37-null, 120 ± 13 pA, $n = 10$) and striatum (*t* test, $P > 0.9999$, WT, 190 ± 10 pA, $n = 10$; exon 37-null, 190 ± 10 pA, $n = 10$). Resting membrane potential was also indistinguishable in cortex (*t* test, $P = 0.55$, W, −62.7 ± 4.8 mV, $n = 10$; exon 37-null, −59.8 ± 4.1 mV, $n = 10$) and striatum (*t* test, $P = 0.99$, WT, −60.7 ± 4.1 mV, $n = 10$; exon 37-null, −60.7 ± 3.2 mV, $n = 10$). AP firing presumably relies not only on precise spatial localization of the voltage-gated channels involved in the upstroke of the spike, but also of other channels and transporters necessary for repolarization of the membrane potential. Consistent with this idea, examination of single APs revealed an increase in the tau for both the rise and decay of the AP consistent with spatial disorganization of the underlying components (Fig. 6 *A* and *B*). In addition, the peak frequency of AP firing was significantly reduced in both the cortex (Fig. 6 *C* and *D*) and striatum (Fig. S7). These data demonstrate that giant AnkG is not necessary for generation of current evoked APs but is essential for proper AP kinetics and peak frequency.

Abnormal Neural Integration in Giant Exon-Knockout Mice. Giant AnkG-null mice exhibit abnormal AP frequency, which would be predicted to impair synchronization of cortical activity that is critical in information processing. In addition, the AIS is a critical site for interneuron synapses, where a single Chandelier interneuron synapses on the AIS of a large number of cortical pyramidal neurons to synchronize their activity (62). To examine synchronized neuronal activity and higher order neuronal function, we performed local field potential recordings from the mouse motor cortex in postnatal day 14 to 16 mice. Alpha oscillations, thought to increase during periods of wakefulness, are more common in giant exon-null mice (Fig. 6*E*). On the other hand, cortical gamma oscillations, associated with higher order cognitive processes such as working memory and conceptual categorization (63), were significantly reduced in the giant exon-null mice relative to their WT littermate controls. This reduction in gamma oscillations is consistent with a reduced rate of spiking, given depolarization, but also suggests a loss of interneuron-mediated neuronal synchronization thought to be critical for oscillations in the gamma range (Fig. 6*F*). Overall, these data demonstrate that loss of 480-kDa AnkG has profound effects on neuronal signaling both at the cellular level, with reduced AP frequency and altered kinetics, and at the circuit level, with altered neuronal synchronization.

Discussion

We demonstrate that assembly of the AIS and normal morphogenesis of CNS nodes of Ranvier both require a heretofore uncharacterized alternatively spliced giant 7.8-kb exon of AnkG. The giant exon was acquired early in vertebrate evolution and resulted in a new nervous system-specific (Fig. S8) 480-kDa polypeptide combining previously known features of ANK repeats and β-spectrin–binding activity with a fibrous domain nearly 150 nm in length imaged by electron microscopy (Fig. 7) (51). We elucidate a previously undescribed function for giant AnkG in recruitment of β4 spectrin to AIS that likely is regulated by phosphorylation at S2417 located within the giant exon-encoded domain. We also demonstrate that 480-kDa AnkG is a major component of the AIS membrane "undercoat' imaged by platinum replica electron microscopy and is required to bundle microtubules at the AIS (51). Surprisingly, giant AnkG-knockout neurons completely lacking known AIS components still generate APs, although with abnormal frequency and altered whole-brain oscillations. Giant AnkG-deficient mice live through weaning and provide a rationale for survival of humans with severe cognitive dysfunction bearing a truncating mutation in the giant exon (41). The giant exon of AnkG thus was a transformative innovation in evolution of the vertebrate nervous system that now is a potential target in neurodevelopmental disorders.

The *ANK2*/*ANK3* ancestral gene likely acquired its giant exon through exon shuffling, a process whereby exons from other genes are duplicated or swapped between already existing genes (64). Giant exons of *ANK2* and *ANK 3* share sequence similarity with I-connectin in a region outside of the FNIII/Ig-like repeats, predominantly with a 2,700 amino acid stretch containing a series of 68 residue SEK repeats (E value 9e−19). The I-connectin SEK domain is passively extensible, with a single SEK repeat behaving as an elastic wormlike chain (65). Interestingly, AnkG imaged at the AIS by platinum replica electron microscopy exhibits a 150-nm length (51) (Fig. 7*C*), which is considerably shorter than the predicted 750 nm if the inserted sequence were an extended unstructured polypeptide, but too long for a single folded domain. Therefore, it is possible that the inserted sequence encoded by the giant exon provides elasticity, perhaps participating in structural support of the AIS. Although *ANK2* (ankyrin-B) and *ANK3* (AnkG) giant exons share extensive sequence similarity along their length, the AnkG exon encodes an additional N-terminal 40 kDa of a serine/threonine-

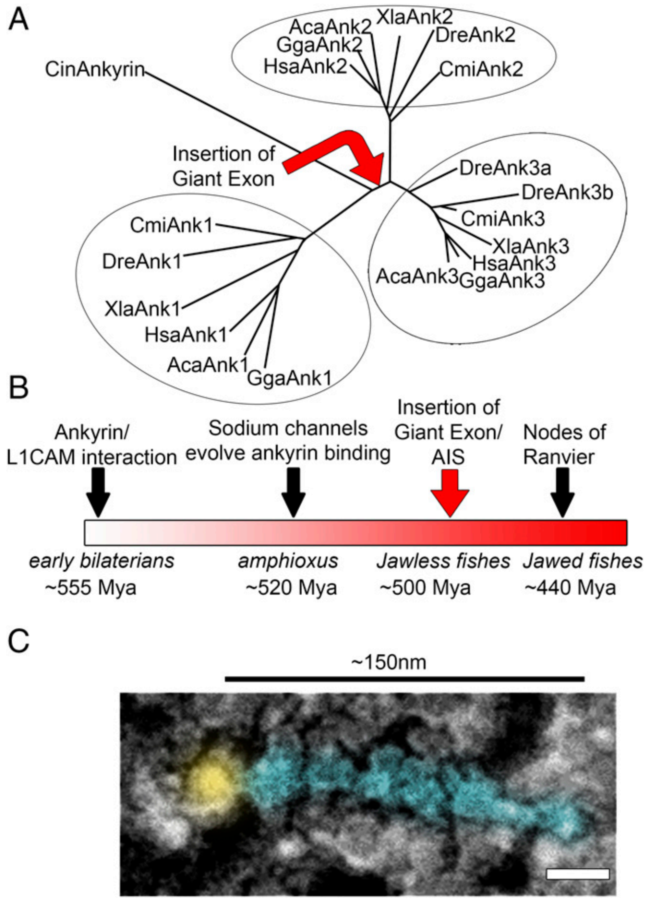

Fig. 7. Insertion of a single conserved exon in vertebrates coincided with formation of the AIS and nodes of Ranvier. (*A*) Rooted phylogenetic tree depicting evolutionary relationships between members of the ankyrin gene family. Arrow represents timing of the insertion of the giant exon 37. Cin, *Ciona intestinalis*; Cmi, *Callorhinchus milii*; Dre, *Danio rerio*; Xla, *Xenopus laevis*; Aca, *Anolis carolinensis*; Gga, *Gallus gallus*; Hsa, *Homo sapiens*. Circled areas denote individual Ank gene groups. (*B*) Relative time of critical steps in the evolution of the nervous system. Insertion of giant exon marked with red arrow. Example organisms shown underneath in italics along with the approximate time of evolution (million years ago). (*C*) Immunogold labeling of AnkG from a platinum replica electron micrograph of an AIS of a cultured rat hippocampal neuron. Gold particle marked in yellow. AnkG molecule marked in cyan. (Scale bar: 25 nm.)

enriched sequence including sites modified by *O*-glucNac (33), as well as regions with sequences quite divergent from ankyrin-B. The ankyrin giant exons, while sharing overall shape and folded domains, likely have evolved distinct molecular partners and functions. It will be useful to explore the hypothesis that the AnkG giant exon-encoded sequence serves as an extended scaffold to recruit multiple proteins, including regulatory components that together are responsible for the specialized characteristics of axonal excitable membranes.

Giant exon-knockout neurons lack all known AIS components and provide a critical test for proposals that the AIS forms a physical barrier that contributes to distinct axonal identity (reviewed in ref. 28). Here, we have found that loss of giant AnkG has profound effects on the proximal axon similar to total knockout of AnkG (18, 26, 27), including loss of the dense fibrillogranular coat and microtubule bundles (Fig. 3), and acquisition of dendritic character in the first 50–100 µm of the axon (Fig. 5 and Figs. S2 and S6). However, after 50–100 µm, distal axo-dendritic polarity resumes in the absence of 480-kDa AnkG, and axonal transport rates of lysosomes were unaffected by the AIS or by axonal position (Fig. 5). These findings support an intrinsic mechanism(s) for establishing and maintaining distinct axonal and dendritic compartments and are consistent with the fact that distinct axonal identity is specified in vivo and in neuronal cultures before establishment of the AIS (60, 66).

Giant exon-null mice still can fire current induced APs and survive until weaning, which was unexpected based on literature concluding that the AIS with its concentration of VGSCs is required to generate APs (reviewed in ref. 61). Possible explanations for persistence of APs in these AIS-deficient mice include contribution from the first node of Ranvier (67) as well as partial compensation due to clustering of VGSCs outside of the AIS induced by increased expression of 190-kDa AnkG (Fig. 3) or recruitment of ankyrin-R (68). These considerations help explain how humans can survive with a truncating mutation of the giant exon of AnkG, at least with institutional support (41).

Alterations in alpha and gamma oscillations in the giant ankyrin-null cortex demonstrate a key role for the giant exon of AnkG in coordination of neuronal network activity. Some of these effects likely result from abnormal AP frequency as well as loss of GABA synapses at the AIS. The 480-kDa AnkG also has recently been discovered to form somatodendritic microdomains in cortical neurons that stabilize cell-surface expression of GABA-A receptors and promote GABAergic synaptogenesis (69). Thus, humans with a mutated or absent AnkG giant exon likely suffer from a major disruption of GABA inhibitory circuits (41). Similarly, missense mutations in giant AnkG associated with autism spectrum disorder may also impair neural circuits. The AnkG giant exon, with its size and nervous system-specific expression (Fig. S8), thus is a potential target for genetic variation affecting cognitive ability, behavior, and neurological function (70).

Materials and Methods

Detailed materials and methods can be found in *SI Materials and Methods*.

A conditional knock-out mouse was made to delete exon 37 of the *ANK3* gene (corresponding to exon 37 of human *ANK3*, ENST00000280772). Exon 37 was flanked by LoxP sites. A neomycin resistance cassette, flanked by flippase recognition target (FRT) sites, was inserted between exon 37 and the 3′ LoxP site. The linearized construct was introduced into 129S6/SvEvTac-derived TL1 embryonic stem (ES) cells by electroporation. ES cells bearing the modified *ANK3* gene were injected into C57BL/6NHsd blastocysts. High percentage chimeric animals were obtained and bred to C57BL/6 mice to produce heterozygous animals. Exon 37 was excised from neuronal and glial precursors by crossing the exon 37 *ANK3* flox mouse with the Nestin-Cre mouse [B6.Cg-Tg(Nes-cre)1Kln/J, stock number 003771; The Jackson Laboratory]. Total AnkG-null mice were generated by crossing the exon 22–23 floxed mouse (44) with the Nestin-Cre mouse. All mouse production was provided by the Duke Cancer Institute Transgenic Mouse Facility. All experiments were performed in accordance with the guidelines for animal care of the Animal Care and Use Program at Duke University.

ACKNOWLEDGMENTS. We acknowledge Kathryn Walder for generating 480-kDa AnkG-GFP plasmid and proposing DAR 480 AnkG experiment, Jonathan Davis for β4 spectrin antibody, Janell Hostettler and Erica Robinson for mouse colony work, and Chirag Vasavda for thoughtful discussions. This work was supported by National Institutes of Health Grant GM095977 (to T.M.S.).

1. Zalc B, Goujet D, Colman D (2008) The origin of the myelination program in vertebrates. *Curr Biol* 18(12):R511–R512.
2. Somogyi P (1977) A specific 'axo-axonal' interneuron in the visual cortex of the rat. *Brain Res* 136(2):345–350.
3. Grubb MS, Burrone J (2010) Activity-dependent relocation of the axon initial segment fine-tunes neuronal excitability. *Nature* 465(7301):1070–1074.
4. Kuba H, Oichi Y, Ohmori H (2010) Presynaptic activity regulates Na(+) channel distribution at the axon initial segment. *Nature* 465(7301):1075–1078.
5. Rasband MN (2010) The axon initial segment and the maintenance of neuronal polarity. *Nat Rev Neurosci* 11(8):552–562.
6. Palay SL, Sotelo C, Peters A, Orkand PM (1968) The axon hillock and the initial segment. *J Cell Biol* 38(1):193–201.

7. Coombs JS, Curtis DR, Eccles JC (1957) The interpretation of spike potentials of motoneurones. *J Physiol* 139(2):198–231.
8. Catterall WA (1984) The molecular basis of neuronal excitability. *Science* 223(4637): 653–661.
9. Srinivasan Y, Elmer L, Davis J, Bennett V, Angelides K (1988) Ankyrin and spectrin associate with voltage-dependent sodium channels in brain. *Nature* 333(6169): 177–180.
10. Kordeli E, Bennett V (1991) Distinct ankyrin isoforms at neuron cell bodies and nodes of Ranvier resolved using erythrocyte ankyrin-deficient mice. *J Cell Biol* 114(6): 1243–1259.
11. Kordeli E, Davis J, Trapp B, Bennett V (1990) An isoform of ankyrin is localized at nodes of Ranvier in myelinated axons of central and peripheral nerves. *J Cell Biol* 110(4):1341–1352.
12. Bennett V (1978) Purification of an active proteolytic fragment of the membrane attachment site for human erythrocyte spectrin. *J Biol Chem* 253(7):2292–2299.
13. Bennett V (1979) Immunoreactive forms of human erythrocyte ankyrin are present in diverse cells and tissues. *Nature* 281(5732):597–599.
14. Bennett V, Stenbuck PJ (1979) The membrane attachment protein for spectrin is associated with band 3 in human erythrocyte membranes. *Nature* 280(5722): 468–473.
15. Bennett V, Stenbuck PJ (1979) Identification and partial purification of ankyrin, the high affinity membrane attachment site for human erythrocyte spectrin. *J Biol Chem* 254(7):2533–2541.
16. Kordeli E, Lambert S, Bennett V (1995) AnkyrinG. A new ankyrin gene with neural-specific isoforms localized at the axonal initial segment and node of Ranvier. *J Biol Chem* 270(5):2352–2359.
17. Jenkins SM, Bennett V (2001) Ankyrin-G coordinates assembly of the spectrin-based membrane skeleton, voltage-gated sodium channels, and L1 CAMs at Purkinje neuron initial segments. *J Cell Biol* 155(5):739–746.
18. Zhou D, et al. (1998) AnkyrinG is required for clustering of voltage-gated Na channels at axon initial segments and for normal action potential firing. *J Cell Biol* 143(5): 1295–1304.
19. Ango F, et al. (2004) Ankyrin-based subcellular gradient of neurofascin, an immunoglobulin family protein, directs GABAergic innervation at purkinje axon initial segment. *Cell* 119(2):257–272.
20. Davis JQ, Bennett V (1994) Ankyrin binding activity shared by the neurofascin/L1/NrCAM family of nervous system cell adhesion molecules. *J Biol Chem* 269(44): 27163–27166.
21. Davis JQ, Lambert S, Bennett V (1996) Molecular composition of the node of Ranvier: Identification of ankyrin-binding cell adhesion molecules neurofascin (mucin+/third FNIII domain-) and NrCAM at nodal axon segments. *J Cell Biol* 135(5):1355–1367.
22. Davis JQ, McLaughlin T, Bennett V (1993) Ankyrin-binding proteins related to nervous system cell adhesion molecules: Candidates to provide transmembrane and intercellular connections in adult brain. *J Cell Biol* 121(1):121–133.
23. Berghs S, et al. (2000) betaIV spectrin, a new spectrin localized at axon initial segments and nodes of ranvier in the central and peripheral nervous system. *J Cell Biol* 151(5):985–1002.
24. Komada M, Soriano P (2002) [Beta]IV-spectrin regulates sodium channel clustering through ankyrin-G at axon initial segments and nodes of Ranvier. *J Cell Biol* 156(2): 337–348.
25. Pan Z, et al. (2006) A common ankyrin-G-based mechanism retains KCNQ and NaV channels at electrically active domains of the axon. *J Neurosci* 26(10):2599–2613.
26. Sobotzik JM, et al. (2009) AnkyrinG is required to maintain axo-dendritic polarity in vivo. *Proc Natl Acad Sci USA* 106(41):17564–17569.
27. Hedstrom KL, Ogawa Y, Rasband MN (2008) AnkyrinG is required for maintenance of the axon initial segment and neuronal polarity. *J Cell Biol* 183(4):635–640.
28. Leterrier C, Dargent B (2014) No Pasaran! Role of the axon initial segment in the regulation of protein transport and the maintenance of axonal identity. *Semin Cell Dev Biol* 27:44–51.
29. Hill AS, et al. (2008) Ion channel clustering at the axon initial segment and node of Ranvier evolved sequentially in early chordates. *PLoS Genet* 4(12):e1000317.
30. Eshed-Eisenbach Y, Peles E (2013) The making of a node: A co-production of neurons and glia. *Curr Opin Neurobiol* 23(6):1049–1056.
31. Bennett V, Lorenzo DN (2013) Spectrin- and ankyrin-based membrane domains and the evolution of vertebrates. *Curr Top Membr* 72:1–37.
32. Pielage J, et al. (2008) A presynaptic giant ankyrin stabilizes the NMJ through regulation of presynaptic microtubules and transsynaptic cell adhesion. *Neuron* 58(2): 195–209.
33. Zhang X, Bennett V (1996) Identification of O-linked N-acetylglucosamine modification of ankyrinG isoforms targeted to nodes of Ranvier. *J Biol Chem* 271(49): 31391–31398.
34. Kunimoto M, Otto E, Bennett V (1991) A new 440-kD isoform is the major ankyrin in neonatal rat brain. *J Cell Biol* 115(5):1319–1331.
35. Chan W, Kordeli E, Bennett V (1993) 440-kD ankyrinB: Structure of the major developmentally regulated domain and selective localization in unmyelinated axons. *J Cell Biol* 123(6 Pt 1):1463–1473.
36. Brachet A, et al. (2010) Ankyrin G restricts ion channel diffusion at the axonal initial segment before the establishment of the diffusion barrier. *J Cell Biol* 191(2):383–395.
37. Yang Y, Ogawa Y, Hedstrom KL, Rasband MN (2007) betaIV spectrin is recruited to axon initial segments and nodes of Ranvier by ankyrinG. *J Cell Biol* 176(4): 509–519.
38. Leterrier C, et al. (2011) End-binding proteins EB3 and EB1 link microtubules to ankyrin G in the axon initial segment. *Proc Natl Acad Sci USA* 108(21): 8826–8831.
39. Zhang X, Bennett V (1998) Restriction of 480/270-kD ankyrin G to axon proximal segments requires multiple ankyrin G-specific domains. *J Cell Biol* 142(6): 1571–1581.
40. He M, Jenkins P, Bennett V (2012) Cysteine 70 of ankyrin-G is S-palmitoylated and is required for function of ankyrin-G in membrane domain assembly. *J Biol Chem* 287(52):43995–44005.
41. Iqbal Z, et al. (2013) Homozygous and heterozygous disruptions of ANK3: At the crossroads of neurodevelopmental and psychiatric disorders. *Hum Mol Genet* 22(10): 1960–1970.
42. Kizhatil K, Bennett V (2004) Lateral membrane biogenesis in human bronchial epithelial cells requires 190-kDa ankyrin-G. *J Biol Chem* 279(16):16706–16714.
43. Song AH, et al. (2009) A selective filter for cytoplasmic transport at the axon initial segment. *Cell* 136(6):1148–1160.
44. Jenkins PM, et al. (2013) E-cadherin polarity is determined by a multifunction motif mediating lateral membrane retention through ankyrin-G and apical-lateral transcytosis through clathrin. *J Biol Chem* 288(20):14018–14031.
45. Ipsaro JJ, Mondragón A (2010) Structural basis for spectrin recognition by ankyrin. *Blood* 115(20):4093–4101.
46. Mohler PJ, Yoon W, Bennett V (2004) Ankyrin-B targets beta2-spectrin to an intracellular compartment in neonatal cardiomyocytes. *J Biol Chem* 279(38): 40185–40193.
47. Kizhatil K, et al. (2007) Ankyrin-G and beta2-spectrin collaborate in biogenesis of lateral membrane of human bronchial epithelial cells. *J Biol Chem* 282(3): 2029–2037.
48. Bréchet A, et al. (2008) Protein kinase CK2 contributes to the organization of sodium channels in axonal membranes by regulating their interactions with ankyrin G. *J Cell Biol* 183(6):1101–1114.
49. Smith KR, et al. (2014) Psychiatric Risk Factor ANK3/Ankyrin-G Nanodomains Regulate the Structure and Function of Glutamatergic Synapses. *Neuron* 84(2):399–415.
50. Peters LL, et al. (1995) Ank3 (epithelial ankyrin), a widely distributed new member of the ankyrin gene family and the major ankyrin in kidney, is expressed in alternatively spliced forms, including forms that lack the repeat domain. *J Cell Biol* 130(2):313–330.
51. Jones SL, Korobova F, Svitkina T (2014) Axon initial segment cytoskeleton comprises a multiprotein submembranous coat containing sparse actin filaments. *J Cell Biol* 205(1):67–81.
52. Susuki K, et al. (2013) Three mechanisms assemble central nervous system nodes of Ranvier. *Neuron* 78(3):469–482.
53. Zonta B, et al. (2008) Glial and neuronal isoforms of Neurofascin have distinct roles in the assembly of nodes of Ranvier in the central nervous system. *J Cell Biol* 181(7): 1169–1177.
54. Tait S, et al. (2000) An oligodendrocyte cell adhesion molecule at the site of assembly of the paranodal axo-glial junction. *J Cell Biol* 150(3):657–666.
55. Zhang X, Davis JQ, Carpenter S, Bennett V (1998) Structural requirements for association of neurofascin with ankyrin. *J Biol Chem* 273(46):30785–30794.
56. Jenkins SM, et al. (2001) FIGQY phosphorylation defines discrete populations of L1 cell adhesion molecules at sites of cell-cell contact and in migrating neurons. *J Cell Sci* 114(Pt 21):3823–3835.
57. Garver TD, Ren Q, Tuvia S, Bennett V (1997) Tyrosine phosphorylation at a site highly conserved in the L1 family of cell adhesion molecules abolishes ankyrin binding and increases lateral mobility of neurofascin. *J Cell Biol* 137(3):703–714.
58. Chang KJ, et al. (2014) Glial ankyrins facilitate paranodal axoglial junction assembly. *Nat Neurosci* 17(12):1673–1681.
59. Winckler B, Forscher P, Mellman I (1999) A diffusion barrier maintains distribution of membrane proteins in polarized neurons. *Nature* 397(6721):698–701.
60. Petersen JD, Kaech S, Banker G (2014) Selective microtubule-based transport of dendritic membrane proteins arises in concert with axon specification. *J Neurosci* 34(12):4135–4147.
61. Kole MH, Stuart GJ (2012) Signal processing in the axon initial segment. *Neuron* 73(2): 235–247.
62. Cobb SR, Buhl EH, Halasy K, Paulsen O, Somogyi P (1995) Synchronization of neuronal activity in hippocampus by individual GABAergic interneurons. *Nature* 378(6552): 75–78.
63. Engel AK, Fries P, Singer W (2001) Dynamic predictions: Oscillations and synchrony in top-down processing. *Nat Rev Neurosci* 2(10):704–716.
64. Patthy L (1999) Genome evolution and the evolution of exon-shuffling: A review. *Gene* 238(1):103–114.
65. Fukuzawa A, et al. (2002) Single-molecule measurement of elasticity of serine-, glutamate- and lysine-rich repeats of invertebrate connectin reveals that its elasticity is caused entropically by random coil structure. *J Muscle Res Cell Motil* 23(5-6):449–453.
66. Galiano MR, et al. (2012) A distal axonal cytoskeleton forms an intra-axonal boundary that controls axon initial segment assembly. *Cell* 149(5):1125–1139.
67. Colbert CM, Johnston D (1996) Axonal action-potential initiation and Na+ channel densities in the soma and axon initial segment of subicular pyramidal neurons. *J Neurosci* 16(21):6676–6686.
68. Ho TS, et al. (2014) A hierarchy of ankyrin-spectrin complexes clusters sodium channels at nodes of Ranvier. *Nat Neurosci* 17(12):1664–1672.
69. Tseng WC, Jenkins PM, Tanaka M, Mooney R, Bennett V (2014) Giant ankyrin-G stabilizes somatodendritic GABAergic synapses through opposing endocytosis of GABAA receptors. *Proc Natl Acad Sci USA* 112:1214–1219.
70. Ferreira MA, et al.; Wellcome Trust Case Control Consortium (2008) Collaborative genome-wide association analysis supports a role for ANK3 and CACNA1C in bipolar disorder. *Nat Genet* 40(9):1056–1058.

Supporting Information

Jenkins et al. 10.1073/pnas.1416544112

SI Materials and Methods

Reagents, Plasmids, and Antibodies. B27 supplement, GlutaMAX, penicillin-streptomycin, Neurobasal A, Hanks' balanced salt solution, trypsin, Hepes, Lipofectamine 2000, and Prolong Gold Antifade Reagent were from Life Technologies. Pipes, gelatin from cold water fish skin, poly-D-lysine, laminin, paraformaldehyde, DNase, phalloidin, taxol, and polyethylene glycol (molecular mass 35 kDa) were from Sigma-Aldrich. Triton X-100 was from MP Biomedicals. BSA was from Gemini Bioproducts. Histochoice clearing agent was from VWR. Tween 20 was from Calbiochem. Electron microscopy-grade glutaraldehyde was from Polysciences.

Rat 190-kDa (1) and 270-kDa (2) ankyrin-G-GFP were previously described. The sequence encoding the giant exon of rat ankyrin-G was identified in the rat genome based on exon 37 of the predicted human transcript of ANK3 (ENST00000280772). This sequence was synthesized by Biomatik including the endogenous ClaI and EcoRV sites found in the 270-kDa ankyrin-G-GFP plasmid and subcloned using ClaI and EcoRV, and the sequence was validated by full-length sequencing across the entire coding region. Mutants for 480-kDa ankyrin-G-GFP were generated using the Quikchange II XL kit (Agilent), subcloned back into 480-kDa ankyrin-G-GFP, and verified by full-length sequencing. For long-term neuronal expression of 190- and 480-kDa ankyrin-G-GFP, the CMV promoter from eGFP-N1 was replaced with a CAG promoter. The numbering of amino acid residues corresponds to the location in human ankyrin-G peptides. Transferrin receptor-YFP and TGN38-YFP were gifts from Antonius M. J. VanDongen, Duke University, Durham, NC. LAMP-1-YFP was purchased from Addgene. Cre-2A-BFP plasmid was generated by cloning Cre recombinase, a viral 2A peptide, and TagBFP under control of a CAG promoter into pLenti6-V5-DEST. The 2A peptide mediates cotranslational cleavage and allows efficient expression of both Cre and BFP. TagBFP-N1 was a generous gift from James Bear, University of North Carolina, Chapel Hill, NC. The 480-kDa ankyrin-G–specific shRNA was generated using the sequence 5′-GAGGTAGAGAGAAGCTGATGT-3′ cloned into pLentilox 3.7 BFP.

Rabbit anti–480-kDa ankyrin-G (2735–2935 of rat 480-kDa ankyrin-G) and rabbit anti-β4 spectrin (800–1094 of mouse β4 spectrin sigma 6, NP_001186163.1) antibodies were generated by cloning the indicated sequences into a pMAL-6xHis-DEST vector. Proteins were expressed in *Escherichia coli* and purified first by nickel chromatography and then by amylose resin. Proteins were cleaved from the amylose resin using Precission Protease (GE Healthcare), covalently coupled to ovalbumin, and injected into rabbits with Freund's complete adjuvant (first injection) and Freund's incomplete adjuvant for all subsequent injections. All rabbit manipulations were performed by Duke Laboratory Animal Resources. Serum was collected, cleared on MBP and ovalbumin columns, and affinity-purified using beads covalently coupled to the original antigen. Finally, antibodies were eluted with 4 M $MgCl_2$ and dialyzed into storage buffer [150 mM NaCl, 10 mM phosphate buffer, 1 mM EDTA, 1 mM NaN_3, and 50% (vol/vol) glycerol]. Goat anti–C-terminal (total) ankyrin-G (3), rabbit anti–C-terminal (total) ankyrin-G (4), and anti-neurofascin FNIII (5) antibodies were previously described. Chicken anti-MAP2 (ab5392) and anti-GFP (ab13970) antibodies were from Abcam. Rabbit anti-GFP antibodies were laboratory-generated. Mouse (S8809) and rabbit (S6936) anti-pan VGSC and mouse anti-MAP2 (M4403) and anti-calbindin (C9848) antibodies were from Sigma-Aldrich. Rabbit anti-KCNQ2 (PA1-929) antibodies were from Thermo Fisher. Guinea pig anti-VGAT (131 004) antibodies were from Synaptic Systems. Mouse anti-Caspr (75-001) antibodies were from Neuromab. All AlexaFluor-conjugated secondary antibodies were from Life Technologies. Pan ankyrin-G antibodies that recognize ankyrin-G, -B, and -R were previously described (6).

Neuronal Culture and Transfection. For hippocampal rescue into an AnkG-null background, exon 22–23 total AnkG floxed mice (7) were maintained as homozygous for the mutant floxed allele. Dissociated hippocampal neurons from flox/flox pups were transfected with Cre-2A-BFP (blue fluorescent protein) plasmid to excise Ank3 in vitro. All experiments were performed in accordance with the guidelines for animal care of the Animal Care and Use Program at Duke University.

Neurons and medium were prepared as described (8). Briefly, hippocampi of postnatal day 0 mouse pups were isolated, treated for 18 min at 37 °C with 0.25% trypsin in HBSS with 10 mM Hepes and 100 μg/mL DNase, and then gently triturated through a glass pipette with a fire-polished tip. The dissociated cells were plated onto poly-D-lysine and laminin-coated MatTek dishes in Neurobasal-A medium containing 10% (vol/vol) FBS, B27 supplement, 2 mM glutamine, and penicillin/streptomycin. On the following day, the medium was replaced with fresh Neurobasal-A medium containing B27, glutamine, penicillin/streptomycin, and 1% FBS.

For rescue of ankyrin-G into an ankyrin-null background, neurons from exon 22–23 flox/flox pups were transfected at DIV3 with Cre-2A-BFP (to excise endogenous ankyrin-G) with or without the rescue plasmid. For Cre-2A-BFP alone, 1 μg of cDNA was used. For 190-kDa and 270-kDa ankyrin-G-GFP rescue, 1 μg of total cDNA was used (0.5 μg of Cre, 0.5 μg of rescue plasmid). For 480-kDa ankyrin-G-GFP and mutant rescue experiments, 1.5 μg of cDNA were used (0.5 μg of Cre, 1.0 μg of rescue plasmid). Briefly, cDNA was added to 100 μL of Neurobasal A, and Lipofectamine 2000 was resuspended in a second tube in 100 μL of Neurobasal A in a 3:1 ratio to cDNA (3-4.5 μL). Tubes were mixed and incubated at room temperature for 15 min. Neuronal growth medium was removed, cells were washed once with Neurobasal A, and transfection mixture was added for 40 min at 37 °C. Transfection mixture was then aspirated, and original growth medium plus 2.5 μg/mL Ara-C was added. Cells were maintained in culture until DIV7 to -9 and imaged live or processed for immunofluorescence as described below.

For DIV21 hippocampal cultures, cells were transfected as described previously (9). Briefly, calcium phosphate transfection was used to introduce DNA/Ca^{2+} phosphate complexes directly onto the cell layer at days 3 in vitro (DIV3). Generally, 1 μg of cDNA in a 25-μL $CaCl_2$/water solution was mixed with 2× Hanks' balanced salt solution followed by gentle vortexing (Clontech). The DNA–Ca^{2+}–phosphate complex was formed after incubation for 15 min at room temperature and then added dropwise to DIV3 neurons prewashed with Neurobasal media on Mat-tek plates. Cells were incubated in a humidified 5% CO_2 chamber at 37 °C for 1 h. Precipitate was dissolved by incubating cells with Neurobasal media preequilibrated in 10% CO_2 in a humidified 5% CO_2 chamber at 37 °C for 20 min. Finally, cells were fed with original growth media containing 2.5 μg/mL Ara-C and maintained until DIV21 for immunofluorescence staining as described below.

Spinal Cord Preparation. For spinal cord immunohistochemistry, P18–P20 were killed by cardiac perfusion, and the spinal cord was immediately removed and fixed overnight in 4% (wt/vol) paraformaldehyde followed by a standard single-day paraffin preparation protocol (PBS wash followed by dehydrations through 70%, 95%, and 100% ethanol with final incubations in xylene and hot paraffin under vacuum). Paraffin sections were cut at 7 μm using a Leica RM2155 microtome. Sections were deparaffinized and rehydrated using a standard protocol of washes: 3 × 3-min Histochoice Clearing Reagent washes, 3 × 2-min 100% ethanol washes, and 1 × 2-min 95%, 80%, and 70% ethanol (each) followed by at least 5 min in PBS. Sections were then processed for antigen retrieval using 10 mM sodium citrate in the microwave for 20 min. Sections were allowed to cool, washed in PBS, and blocked using blocking buffer. Slides were incubated overnight at 4 °C with primary antibodies diluted in blocking buffer. After extensive PBS washing, slides were incubated in blocking buffer with the appropriate secondary antibodies for 1 h at room temperature, washed, and mounted with Prolong Gold Antifade reagent.

Immunofluorescence. For all antibodies except pan VGSC, dissociated hippocampal neurons were fixed for 15 min at room temperature with 4% (wt/vol) paraformaldehyde, permeabilized for 10 min with 0.2% Triton X-100 in PBS, and blocked with blocking buffer [5% (wt/vol) BSA, 0.2% Tween 20] in PBS. Primary antibodies were diluted in blocking buffer and incubated overnight at 4 °C. For mouse pan VGSC, cells were fixed for 15 min at room temperature with 4% (wt/vol) paraformaldehyde and permeabilized and blocked simultaneously with gelatin buffer [5% (wt/vol) fish gelatin, 0.25% Tween in PBS] for 30 min at room temperature. Primary antibodies were diluted in gelatin buffer and incubated for 2 h at room temperature. All cells were washed with PBS, incubated with secondary antibodies diluted in blocking buffer for 1–2 h at room temperature, washed, and mounted with Prolong Gold.

For immunohistochemistry, P18–P20 were killed by cardiac perfusion, and brain was immediately removed and fixed overnight in 4% (wt/vol) paraformaldehyde followed by a standard single day paraffin preparation protocol (PBS wash followed by dehydrations through 70%, 95%, and 100% ethanol with final incubations in xylene and hot paraffin under vacuum). Paraffin sections were cut at 7 μm using a Leica RM2155 microtome. Sections were deparaffinized and rehydrated using a standard protocol of washes: 3 × 3-min Histochoice Clearing Reagent washes, 3 × 2-min 100% ethanol washes, and 1 × 2-min 95%, 80%, and 70% ethanol (each) followed by at least 5 min in PBS. Sections were then processed for antigen retrieval using 10 mM sodium citrate in the microwave for 20 min. Sections were allowed to cool, washed in PBS, and blocked using blocking buffer. Slides were incubated overnight at 4 °C with primary antibodies diluted in blocking buffer. After extensive PBS washing, slides were incubated in blocking buffer with the appropriate secondary antibodies for 1 h at room temperature, washed, and mounted with Prolong Gold Antifade reagent.

The following antibody dilutions were used: anti–480-kDa ankyrin-G (1:500), anti–total ankyrin-G (1:500), chicken or mouse anti-MAP2 (1:1,000), mouse anti-pan VGSC (1:100, for dissociated hippocampal cultures), rabbit anti-pan VGSC (1:100, for brain slices), rabbit anti-β4 spectrin (1:500), rabbit anti-GFP (1:1,000), rabbit anti-neurofascin (1:500), mouse anti-Caspr (1:1,000), guinea pig anti-VGAT (1:1,000), mouse anti-calbindin (1:1,000), rabbit anti-KCNQ2 (1:250), and all secondary antibodies (1:250).

Confocal Microscopy and Live Imaging. Samples were imaged on a Zeiss LSM 780 with a 40 × 1.3 Plan-Apochromat objective, and excitation was accomplished using 405-, 488-, 561-, and 633-nm lasers. For live imaging experiments, a humidified, temperature-controller chamber was used to maintain the neuronal cultures at 37 °C and 5% CO_2 in physiological salt solution (141 mM CaCl, 5.6 mM KCl, 2.2 mM $CaCl_2$, 0.5 mM $MgCl_2$, 5.6 mM glucose, 15 mM Hepes, pH 7.4).

Electron Microscopy. Hippocampal cultures grown on MatTek dishes were prepared essentially as described previously (10). Cells were extracted for 3 min with 1% Triton X-100, 2% (vol/vol) PEG-35,000, 2 μM phalloidin, 2 μM taxol in PEM buffer (100 mM Pipes, pH 6.9, 5 mM EGTA, 5 mM $MgCl_2$) at room temperature. Cells were washed three times with PEM buffer containing 2 μM phalloidin and 2 μM taxol and then fixed in 2% (vol/vol) glutaraldehyde in 0.1 M sodium cacodylate, pH 7.3 for 20 min at room temperature. Coverslips were then removed from the dish and prepared for electron microscopy and imaged as described previously (10). In brief, detergent-extracted samples were fixed with 2% (vol/vol) glutaraldehyde, tannic acid, and uranyl acetate; critical point dried; coated with platinum and carbon; and transferred onto electron microscopic grids for observation. Samples were examined using a transmission electron microscope (JEM 1011; JEOL) operated at 100 kV. Images were acquired by a charge-coupled device camera (ORIUS 832.10W; Gatan) and presented in inverted contrast. Gold particles in replica electron microscopy images were identified at high magnification after contrast enhancement to distinguish them from other bright objects in the samples.

Western Blot. Mouse brains were dissected and hand-dounced on ice in 10 volumes/weight homogenization buffer (10 mM phosphate buffer, pH 7.4, 0.32 M sucrose, 1 mM EDTA, 1 mM NaN_3, plus protease inhibitors), mixed 1:1 with 5× PAGE buffer [5% (wt/vol) SDS, 25% (wt/vol) sucrose, 50 mM Tris, pH 8, 5 mM EDTA, bromophenol blue], sonicated 10 pulses, and heated to 65 °C for 10 min. Samples (10-μL volume) were run on a 3.5–17.5% gradient gel in 1× Tris buffer, pH 7.4 (40 mM Tris, 20 mM NaOAc, and 2 mM NaEDTA) with 0.2% SDS (11). Transfer to nitrocellulose was performed overnight at 300 mA at 4 °C in 0.5× Tris buffer with 0.01% SDS. Membranes were blocked with Blot buffer I (150 mM NaCl, 1 mM NaN_3, 1 mM EDTA, 0.2% Triton X-100, and 10 mM phosphate buffer, pH 7.4) with 2% (wt/vol) BSA and incubated overnight at 4 °C with primary antibodies (rabbit total ankyrin-G, 1:5,000) diluted in blocking buffer. Membranes were then incubated with I125-labeled protein A/G (1:1,000). Membranes were placed on a storage phosphor screen, and signal was detected using a Typhoon imager (GE Healthcare).

In Vitro Electrophysiology Recording and Analysis. For whole-cell patch-clamp recordings, brains from animals (WT, 3; KO, 3) were removed quickly into ice-cold solution bubbled with 95% O2–5% CO_2 containing the following: sucrose (194 mM), NaCl (30 mM), KCl (2.5 mM), $MgCl_2$ (1 mM), $NaHCO_3$ (26 mM), NaH_2PO_4 (1.2 mM), and D-glucose (10 mM). After 4–5 min, the brains were blocked, and coronal slices were taken at 250 μm. During the recovery period (30 min), the slices were placed and stabilized at 35.5 °C with oxygenated artificial cerebrospinal fluid (aCSF) solution containing the following: NaCl (124 mM), KCl (2.5 mM), $CaCl_2$ (2 mM), $MgCl_2$ (1 mM), $NaHCO_3$ (26 mM), NaH_2PO_4 (1.2 mM), and D-glucose (10 mM) with pH adjusted to 7.4 with HCl and osmolarity set to 319 mosM. Internal solution for the pipette (3–5 MΩ) contained: potassium gluconate (150 mM), $MgCl_2$ (2 mM), EGTA (1.1 mM), Hepes (10 mM), sodium ATP (3 mM), and sodium GTP (0.2 mM) with pH adjusted to 7.2 with KOH and osmolarity set to 315 mosM. All recordings were performed under continuous perfusion of aCSF at 28–29 °C with 2–3 mL/min flow rate, and with a MultiClamp 700B amplifier (Molecular Device). To measure neuronal excitability, current-clamp recording was performed from coronal mouse brain slices. Recorded signals were filtered at 10 kHz and digitized at

20 kHz with a Digidata 1440A digitizer (Molecular Devices). Data were analyzed using pCLAMP10 (Molecular Devices).

In Vivo Electrophysiology Recording and Analysis. Surgery (WT, 2; Exon 37-null, 3) was performed under anesthesia with isoflurane (2%). A craniotomy was performed over the motor cortex locations according to known stereotaxic coordinates [from bregma in µm, the coordinates were anteroposterior (AP) 1.1 and mediolateral (ML) 1.2]. The electrode arrays used in this study consisted of custom-made 2 × 8 platinum-coated tungsten microwire electrodes (35 µm diameter) with 150 µm between microwires, and 200 µm between rows. The arrays were lowered to the appropriate stereotaxic depth (~1 µm) to target layer 5 in the primary motor cortex and fixed in place with dental acrylic. After 6 h, we started recording local field potentials (LFPs, five sessions from KO and four sessions from WT, each session lasting at least 10 min). LFP signals were filtered with a third order high-pass filter and seventh order low-pass filter (0.1-Hz to 5-Hz cutoffs). The analysis of LFP power was performed using Neuroexplorer. The power spectra were calculated using Welch's method (512 frequencies between 1 and 55 Hz). Alpha and gamma were defined as 8–15 Hz and 30–55 Hz in frequency, respectively. In addition, electrode placement was verified postmortem after fixation with 10% (vol/vol) formalin, followed by thionin staining in 100-µm coronal sections.

Phylogenetic Analysis. Alignment of the ankyrin family was done using ankyrin sequences with the giant exon removed to accurately compare homology of ankyrin-R (which does not contain a giant insert) with ankyrin-B and ankyrin-G. Alignments were performed using the ClustalW2 website (www.ebi.ac.uk/Tools/msa/clustalw2/), and the resulting alignments were used to generate a rooted phylogenetic tree (iubio.bio.indiana.edu/treeapp/treeprint-form.html).

qRT-PCR. For gene-expression studies, animals were killed by decapitation, and tissues were quickly dissected and frozen in liquid nitrogen. Total RNA was isolated using RNeasy mini kit (Qiagen) according to the manufacturer's instructions. First strand synthesis was carried out using SuperScript III reverse transcriptase (Life Technologies). Quantitative RT-PCR (qRT-PCR), duplex primer-probe PrimeTime assays (IDT) were designed to span exon–exon boundaries to specifically amplify 190-kDa or 480-kDa ankyrin-G. For 190-kDa ankyrin-G, the primer sequences were 5′-GCTTTGCCTCCCTAGCTTTA-3′ and 5′- GATATCCGTCCGCTCACAAG-3′ and the probe was 5′- TTGACTGAACCCAGCATGAGTCCG-3′. For 480-kDa ankyrin-G, the primer sequences were 5′-GAGGCACCGCCCTTAAA-3′ and 5′-GCCAGCTCTGTCCAACTAA-3′ and the probe was 5′-AGAGTCCTTGTGAGCGGACGGATA-3′. Ankyrin-G probes were Zen-modified and FAM-labeled, and standard GAPDH probes were Zen-modified and HEX labeled. RT-PCR was performed in duplex using TaqMan Gene Expression Master Mix (Applied Biosystems) and a StepOnePlus PCR system (Life Technologies) according to the manufacturer's instructions.

Statistical and Data Analysis. Measurements were taken using Zeiss Zen or NIH ImageJ software and repeated for at least three independent experiments. Statistical analysis was performed using Graphpad Prism software. For quantification of axon initial segment (AIS) density, a background subtracted value for the region of interest corresponding to the AIS of the transfected neuron was expressed as a ratio to a corresponding region of interest from a nearby nontransfected (WT) neuron. Data shown are mean ± SEM. Student's *t* test was used for comparisons between two groups whereas a one-way ANOVA with Tukey post hoc test was used to compare three or more groups.

1. Kizhatil K, Bennett V (2004) Lateral membrane biogenesis in human bronchial epithelial cells requires 190-kDa ankyrin-G. *J Biol Chem* 279(16):16706–16714.
2. Zhang X, Bennett V (1998) Restriction of 480/270-kD ankyrin G to axon proximal segments requires multiple ankyrin G-specific domains. *J Cell Biol* 142(6):1571–1581.
3. He M, Abdi KM, Bennett V (2014) Ankyrin-G palmitoylation and βII-spectrin binding to phosphoinositide lipids drive lateral membrane assembly. *J Cell Biol* 206(2):273–288.
4. Kizhatil K, et al. (2007) Ankyrin-G and beta2-spectrin collaborate in biogenesis of lateral membrane of human bronchial epithelial cells. *J Biol Chem* 282(3):2029–2037.
5. Davis JQ, Lambert S, Bennett V (1996) Molecular composition of the node of Ranvier: identification of ankyrin-binding cell adhesion molecules neurofascin (mucin+/third FNIII domain-) and NrCAM at nodal axon segments. *J Cell Biol* 135(5):1355–1367.
6. Bennett V (1979) Immunoreactive forms of human erythrocyte ankyrin are present in diverse cells and tissues. *Nature* 281(5732):597–599.
7. Jenkins PM, et al. (2013) E-cadherin polarity is determined by a multifunction motif mediating lateral membrane retention through ankyrin-G and apical-lateral transcytosis through clathrin. *J Biol Chem* 288(20):14018–14031.
8. He M, Jenkins P, Bennett V (2012) Cysteine 70 of ankyrin-G is S-palmitoylated and is required for function of ankyrin-G in membrane domain assembly. *J Biol Chem* 287(52):43995–44005.
9. Tseng WC, Jenkins PM, Tanaka M, Mooney R, Bennett V (2014) Giant ankyrin-G stabilizes somatodendritic GABAergic synapses through opposing endocytosis of GABAA receptors. *Proc Natl Acad Sci USA*, 10.1073/pnas.1417989112.
10. Jones SL, Korobova F, Svitkina T (2014) Axon initial segment cytoskeleton comprises a multiprotein submembranous coat containing sparse actin filaments. *J Cell Biol* 205(1):67–81.
11. Bennett V, Davis J (1981) Erythrocyte ankyrin: Immunoreactive analogues are associated with mitotic structures in cultured cells and with microtubules in brain. *Proc Natl Acad Sci USA* 78(12):7550–7554.

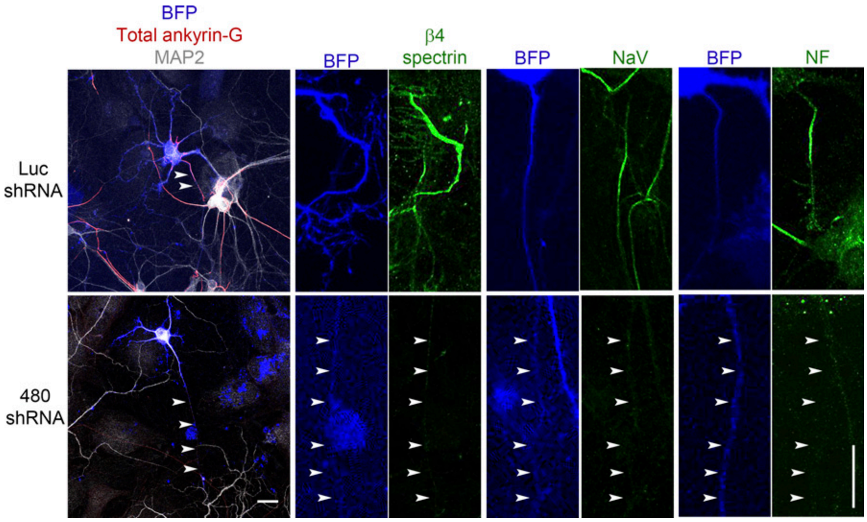

Fig. S1. The 480-kDa ankyrin-G–specific shRNA completely abolishes clustering of known AIS proteins in the proximal axon. Representative images from cultured hippocampal neurons expressing a control shRNA to luciferase (*Top*) or shRNA to 480-kDa ankyrin-G. BFP shown in blue, total ankyrin-G staining shown in red. MAP2 shown in white. (Scale bar: 20 μm.) Higher magnification images of axon shown on *Right* for BFP (blue) and either β4 spectrin, VGSC, or NF (green).

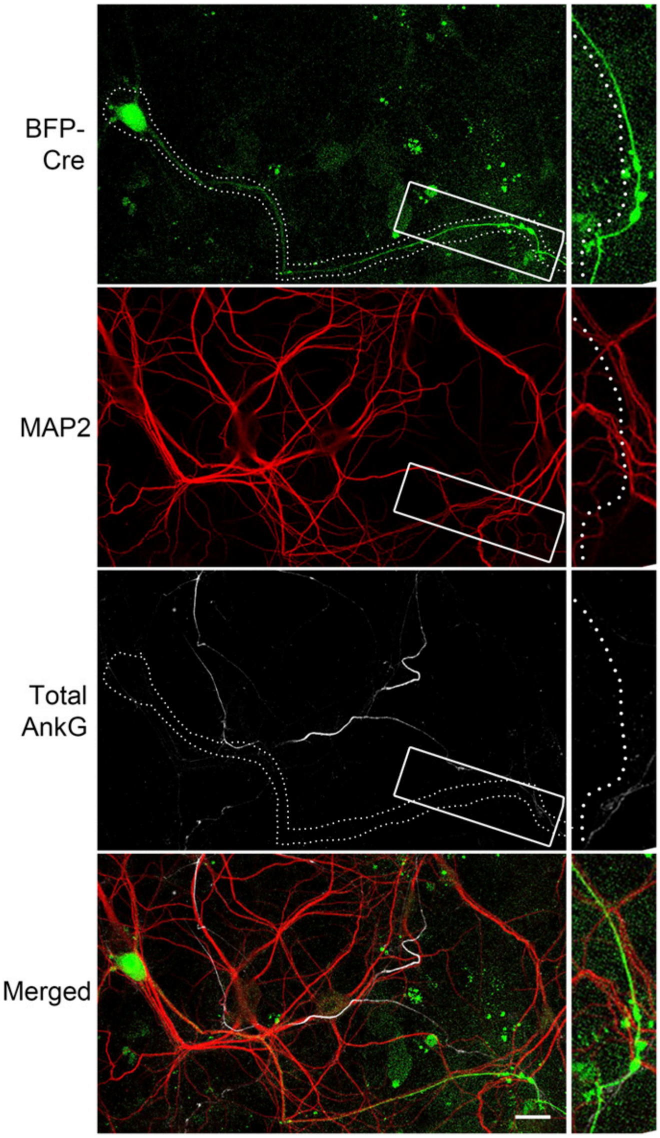

Fig. S2. Cre transfection at DIV3 completely abolishes ankyrin-G clustering at AIS by DIV7. Representative images of a cultured exon 22–23 flox/flox hippocampal neurons transfected with Cre-2A-BFP (pseudocolored green). MAP2 is shown in red, and total ankyrin-G staining is shown in white. Higher magnification of distal axon region of interest shown on *Right*. (Scale bar: 20 μm.)

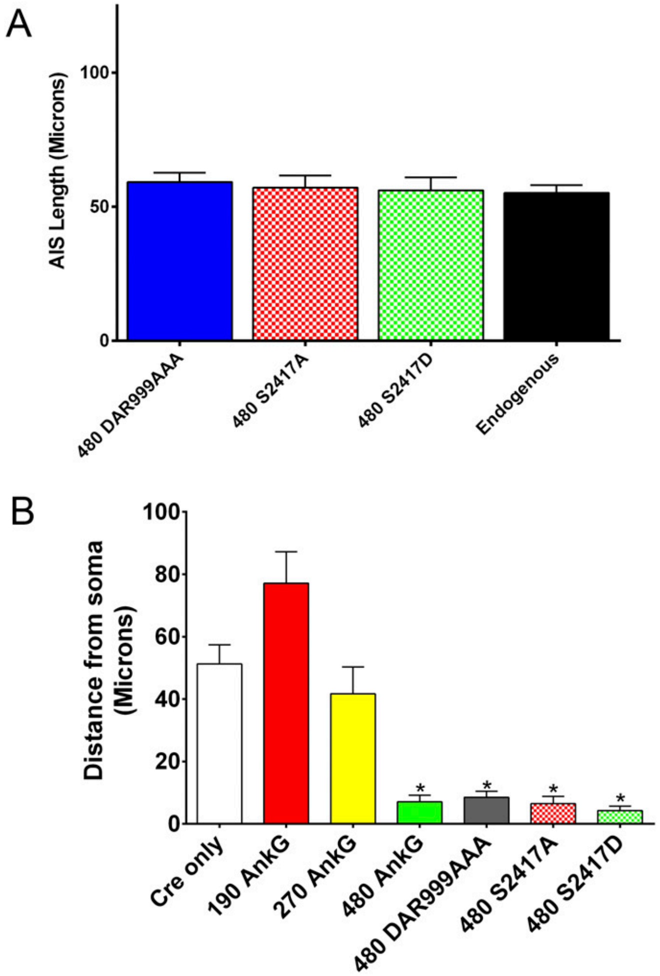

Fig. S3. Measurements of cluster length and AIS position relative to endogenous AIS. (*A*) Average measurements of AIS clustering of 480-kDa ankyrin-G-GFP with the indicated mutations relative to endogenous AIS ($P = 0.9099$, one-way ANOVA, $n = 18$–21 per group). (*B*) Average distance from soma for transition between dendritic character (MAP2-positive) and axonal character (MAP2-negative) in total ankyrin-G–null neurons rescued with the indicated constructs. ($P < 0.0001$, one-way ANOVA followed by Tukey post hoc test; $^*P < 0.05$ relative to total ankyrin-G–null, Cre only).

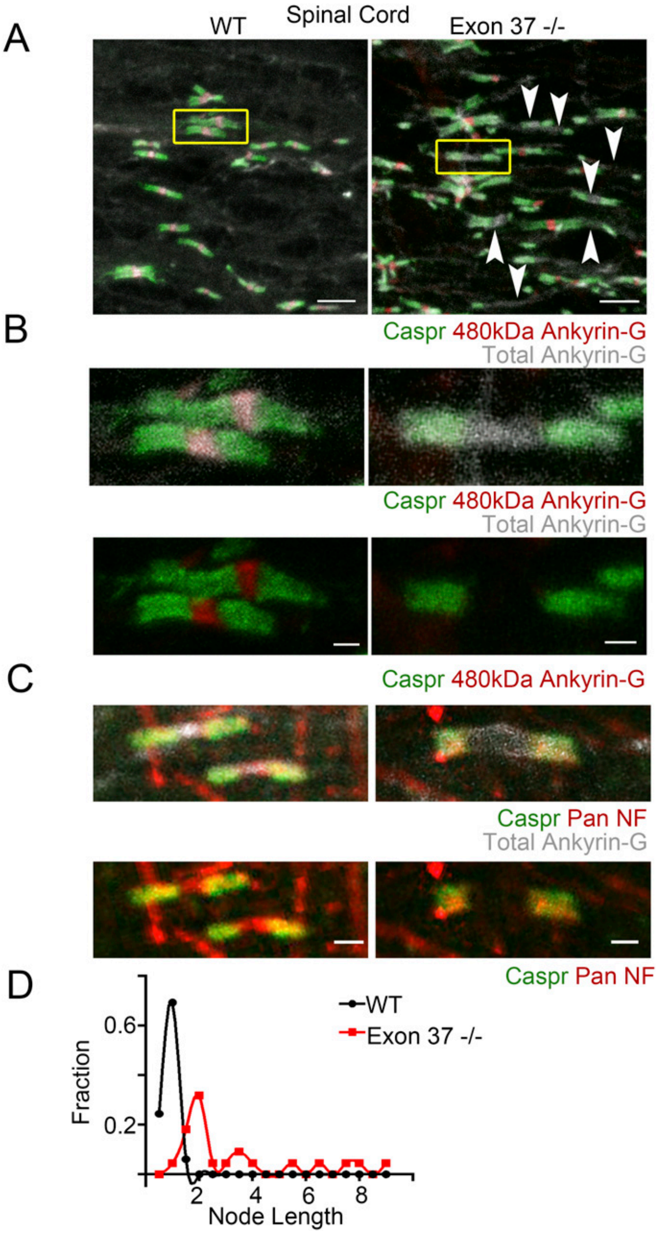

Fig. S4. A subset of nodes of Ranvier in the spinal cord are affected by nestin-Cre–mediated deletion of exon 37. (*A*) Representative images of sections through spinal cord from p20 WT or exon 37-null mice. Sections were stained with antibodies to the paranode marker Caspr (green), 480-kDa ankyrin-G (red), and total ankyrin-G (white). (Scale bars: 5 μm.) (*B*) Higher magnification of nodes of Ranvier from yellow regions of interest in *A*. (Scale bars: 1 μm.) (*C*) Higher magnification images of nodes from WT or exon 37-null mice. Caspr (green), NF (red), and total ankyrin-G (white). (Scale bars: 1 μm.) (*D*) Histogram of node of Ranvier length from WT (black) or exon 37-null (red) nodes of Ranvier from p20 spinal cord. Nodes were determined to be exon 37-null by loss of 480-kDa AnkG staining.

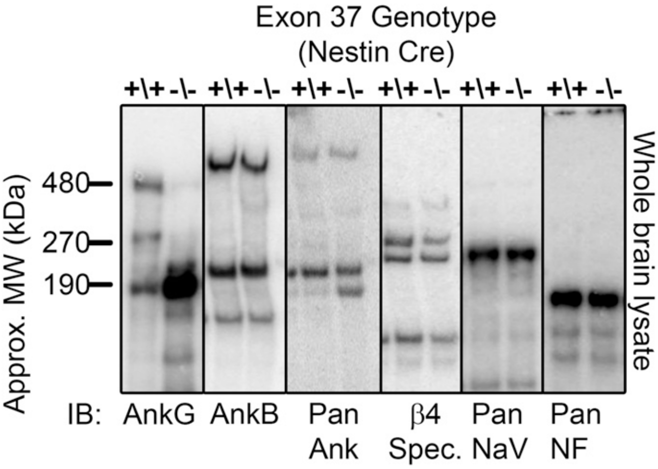

Fig. S5. No changes detected in protein expression of other ankyrin isoforms or known ankyrin-G partners. Western blot analysis from whole-brain lysate of P20 WT (+/+) or exon 37-null (–/–) animals. Blots were probed with antibodies to total ankyrin-G (AnkG), total ankyrin-B (AnkB), pan ankyrin (Pan Ank), β4 spectrin, pan voltage-gated sodium channel (Pan NaV), and Pan neurofascin (Pan NF).

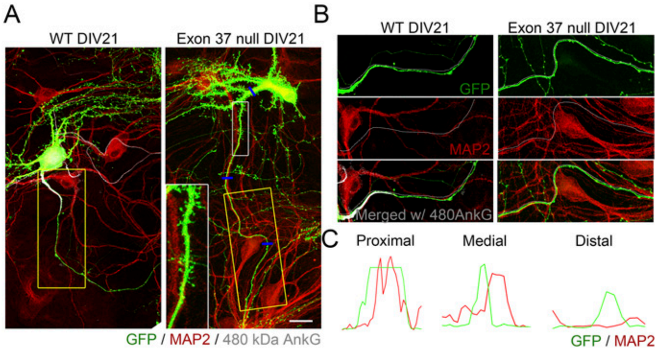

Fig. S6. DIV21 Exon 37-null hippocampal neurons exhibit profound proximal axon polarity defects but maintain distal polarity. (*A*) Representative images of WT (*Left*) or exon 37-null (*Right*) DIV21 cultured hippocampal neurons. Soluble GFP shown in green. MAP2 shown in red. Staining for 480-kDa ankyrin-G staining shown in white. (Scale bar: 20 mμ.) Blue bars represent position of line scan analysis shown in *C*. Exon 37-null *Inset* demonstrates acquisition of dendrites in proximal axon. (*B*) Higher magnification images of yellow regions of interest shown in *A* demonstrating loss of MAP2 in distal axon of exon 37-null neuron. (*C*) Line fluorescent intensity analysis of blue bars shown in *A* in proximal, medial, or distal axon. GFP shown in green. MAP2 shown in red.

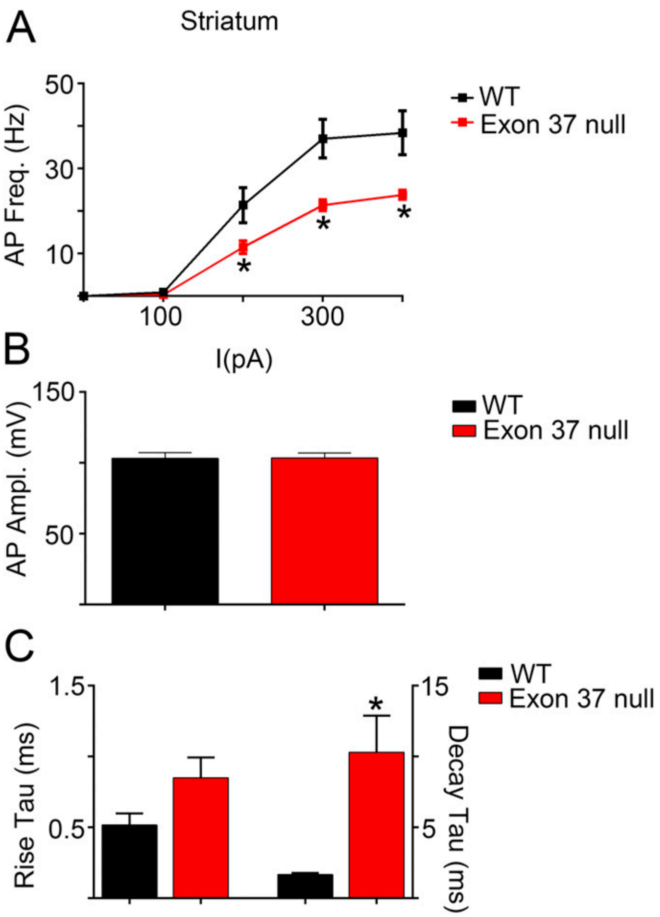

Fig. S7. Action potential frequency and dynamics are affected in the striatum of the exon 37-null mouse. (*A*) Elicited action potential frequency from striatal neurons from WT (black) or exon 37-null (red) acute brain slices. Data shown are mean ± SEM, $*P < 0.05$ compared with WT. (*B*) Action potential amplitude from WT (black) or exon 37-null (red) striatal neurons at +400 pA current injection (WT, 103.2 ± 4.050 mV, $n = 10$; exon 37-null, 103.5 ± 3.532 mV, $n = 10$). (*C*) Time constants (τ) for action potential rise (*Left*) or decay (*Right*) from WT (black) or exon 37-null (red) striatal neurons at +400 pA current injection (rise τ, $P = 0.0586$; WT, 0.5 ± 0.1 ms, $n = 10$; exon 37-null, 0.9 ± 0.1, $n = 10$; decay τ, $*P = 0.0036$; WT, 1.7 ± 0.1 ms, $n = 10$; exon 37-null, 10.3 ± 2.6 ms, $n = 10$).

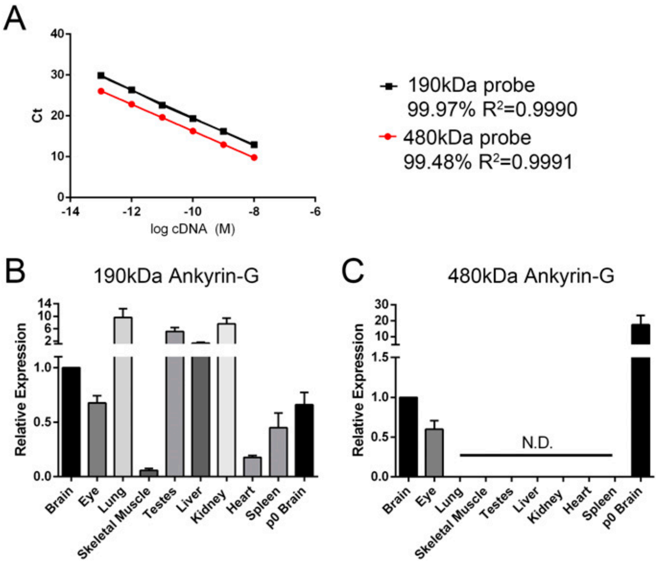

Fig. S8. The 480-kDa ankyrin-G expression is restricted to neuronal tissues. (*A*) Probe validation for qRT-PCR probes specific for 190-kDa (black) or 480-kDa (red) ankyrin-G using cDNA encoding each isoform as a template. (*B*) Relative190-kDa ankyrin-G gene expression from P30 WT mouse tissues or P0 brain. Data normalized to GAPDH as endogenous control and to P30 brain. (C) Relative 480-kDa ankyrin-G gene expression from P30 WT mouse tissues or P0 brain. Data normalized to GAPDH as endogenous control and to P30 brain.